METEORITICS & PLANETARY SCIENCE

Micro-imaging Spectroscopy and Scanning Electron Microscopy of Northwest Africa 8657- shergottite: interpretation of future in situ Martian data.

Journal:	*Meteoritics & Planetary Science*
Manuscript ID	MAPS-2854.R3
Manuscript Type:	Article
Date Submitted by the Author:	n/a
Complete List of Authors:	Manzari, Paola; Istituto di Astrofisica e Planetologia Spaziali, De Angelis, Simone; Istituto di Astrofisica e Planetologia Spaziali De Sanctis, Maria Cristina; Inaf, IAPS Agrosì, Giovanna; Universita degli Studi di Bari Aldo Moro Dipartimento di Scienze della Terra e Geoambientali Tempesta, Gioacchino; Universita degli Studi di Bari Aldo Moro Dipartimento di Scienze della Terra e Geoambientali
Keywords:	Martian meteorite(s), Micro-imaging VIS-IR, MaMISS, Spectral reflectance

Micro-imaging Spectroscopy and Scanning Electron Microscopy of Northwest Africa 8657- shergottite: Interpretation of future *in situ* Martian data.

[1]Manzari P., [1]De Angelis S., [1]De Sanctis M.C., [2]Agrosì G., [2]Tempesta G.

[1] Istituto di Astrofisica e Planetologia Spaziali, INAF-IAPS, via Fosso del Cavaliere, 100 – 00133, Roma, Italy;
[2] Dipartimento di Scienze della Terra e Geoambientali (DiSTeGeo), University of Bari, Via E. Orabona 4, 70125, Bari, Italy

Corresponding author: paola.manzari@iaps.inaf.it

Abstract

Micro-imaging spectroscopy is going to be the new frontier for validating reflectance remote sensed data from missions to Solar System bodies. In this field, micro-imaging spectroscopy of Martian meteorites can provide important and new contributions to interpret data that will be collected by next instruments onboard rover missions to Mars, such as for example Exomars-2020/Ma_MISS spectrometer. In this paper, a slab from the North West Africa (NWA) 8657 shergottite was studied using the SPectral IMager (SPIM) micro-imaging spectrometer, in the visible-infrared (VIS-IR) range, with the aim to subsequently validate the spectral data by means of different independent techniques. The validation was thus carried out, for the first time, comparing SPIM spectral images, characterized by high spatial and spectral resolution, with mineralogical-petrological analyses, obtained by Scanning Electron Microscopy (SEM).

The suitability of the SPIM resolution to detect and map augite, pigeonite, maskelynite and other minor phases as calcite, Ca-phosphates, and troilite/pyrrhotite with no loss of information about mineral distribution on the slab surface, was ascertained. The good agreement found between spectral and mineralogical data suggests that spectral-petrography of meteorites may be useful to support in-situ investigations on Martian rocks carried out by MaMiss spectrometer during Exomars2020 mission. Moreover, micro spectral images could be also useful to characterize, in non-destructive way, Martian meteorites and other rare minerals occurring in meteorites. The results obtained in this work represent not only a methodological contribution to the study of meteorites, but furnish also elements to reconstruct the history of this sample. The finding of zoned pyroxene, symplectitic texture, amorphous phases as maskelynite and Fe-merrillite permit to hypothesized four stages: 1) igneous formation of rimmed pyroxenes and other minerals, 2) retrograde metamorphism, 3) shock by impact and 4) secondary minerals by terrestrial contamination.

Introduction

Martian meteorites represent currently the only chance to directly analyze samples from Mars. Martian meteorites are a group of achondritic meteorites that are distinct in terms of their mineral chemistry, oxidation-reduction state (higher oxygen fugacity), oxygen isotope composition, and radiometric ages (McSween 1985, 2002). The most direct evidence about their origin is the similarity of the isotopic composition of noble gases found as gas inclusions in impact-melted glass to the modern Martian atmospheric values (e.g., Treiman *et al.* 2000). The N and Ar isotope compositions fall on a mixing line between the composition of the Martian and terrestrial atmosphere (Bogard and Johnson 1983; Bogard *et al.* 1984). Visible to infrared (VIS-IR) spectroscopy of Martian meteorites has been extensively used for validation of remotely sensed data from Mars. Recently, visible to infrared microimaging spectroscopy provided simultaneous fine-scale composition (mineralogy, ices, and organics) and imaging at a grain scale (e.g. Manzari *et al.*, 2016; Ehlmann *et al.*, 2016; Greenberger *et al.*, 2015; Cannon *et al.*, 2015). Ma_MISS (Mars Multispectral Imager for Subsurface Studies) onboard the ExoMars 2020 spacecraft (Coradini, A. *et al.*, 2001; De Sanctis *et al.*, 2017) will be the first spectrometer that will study the Martian subsurface *in situ* to a depth of 2 meters. The Ma_MISS is a miniaturized spectrometer, integrated within the drilling system of the ExoMars rover; it will perform visible and near infrared spectroscopy in the 0.4-2.2 μm range, acquiring signal from the excavated borehole wall with 120 μm spatial resolution. Consecutive adjacent acquisitions will permit reconstruction of column and ring images of the excavated borehole. Imaging spectroscopy investigations of Martian meteorites can provide significant contributions to the interpretation of images and spectral data that will be collected by the Ma_MISS on Mars surface. Martian meteorites have been largely investigated by means of VIS-NIR reflectance spectroscopy, using low resolution spectrometers. For example, Schade and Wasch, (1999) analyzed the NIR spectral properties of bulk samples of Zagami and Nakhla with the aim of supporting the remote investigations of the Martian crust. McFadden and Cline (2005) studied 9 Martian meteorites using the visible and near infrared range (0.36-2.5 μm) with the goal to link the band parameters of the spectral signatures of powdered samples of 6 shergottites, 2 nakhlites and 1 chassygnite to the possible Mars source region of these meteorites. Hiroi *et al.*, (2011) analyzed 8 shergottites and 4 nakhlites chips stored at National Institute of Polar Research in the range between 0.25- 2.5 μm with the aim to validate Mars rover' data and to quickly characterize Martian meteorites.

The validation of these previous spectral measurements consisted of mineralogical characterization by optical microscopy of thin sections and by X-ray Powders Diffraction (XRPD) and X-ray fluorescence (XRF), typically performed on grinded and sieved powders obtained from whole rock, assuming these samples as representative of the investigated surface. Nevertheless, this approach does not allow an exact assignment of each acquired reflectance spectrum to the corresponding phase. Spectral deconvolution instead needs the individual contributions of different phases (i.e. endmembers) within a mixing to be identified and separated. Spectrally inactive or featureless mineral phases, together with the overlapping of absorption bands makes the interpretation of spectra of mixture far more complex.

In the present paper, visible and infrared micro-spectroscopy data acquired on the NWA8657 shergottite slab, are reported. The original contribution of this paper, with respect to the previous studies on shergottites, regards the possibility to perform high spatial resolution (tens of micrometers) spectral investigations by using SPIM imaging facility (De Angelis *et al.*, 2015), preserving the information about the spatial distribution of minerals on the slab surface. In fact, this technique is not destructive and needs no preparation of the samples, allowing obtaining useful clues for the interpretation of the geological settings of data from remote sensing. Moreover, the non-destructive nature permits preservation of the intrinsic value of the extraterrestrial materials, to reproduce the analyses and to collect data by a multi-analytical approach. The visible-infrared microimaging spectroscopy has high potential for meteorite studies, where samples are rare and thus the ability to obtain mineralogical information non-destructively is desirable. The validity of SPIM imaging spectrometer facility was recently proved and confirmed by Manzari *et al.* (2016) in a study on Mars analogues at sub-millimeter scale. This facility allows collection of data with a spatial resolution of about 38 μm/pixel in the spectral range 0.25-5 μm (De Angelis *et al.*, 2015).

The sample studied in this paper is a coarse-grained basaltic shergottite fragment that was found in Northwest Africa – (NWA 8657) in 2014 (Meteoritical Bulletin, 2014). It is about 4x10 mm in size, with a thickness of about 2 mm (Fig.1).

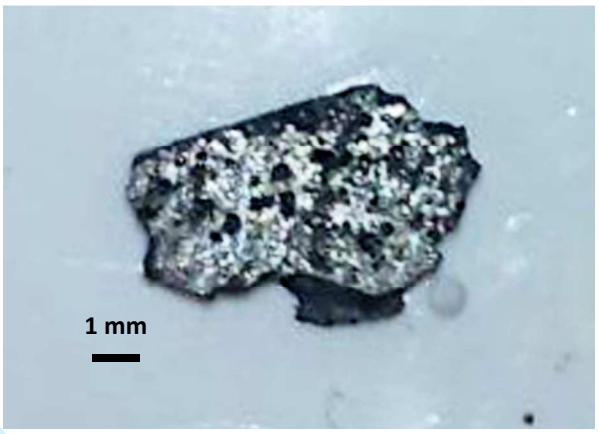

Fig.1. Picture of North West Africa 8657 slab

According to the classification of Meteoritical Bulletin (2014), this shergottite shows a diabasic texture, and consists mainly of clinopyroxene and amorphous phases with plagioclasic composition (maskelynite), with accessory phases such as iron oxides (i.e. ulvospinel), iron monosulfides (pyrrothite/troilite), Ca phosphates (Fe-merrillite-whitlockite and chlorapatite) and vesicular glass. The formation mechanism of maskelynite is still debated (Jaret *et al*., 2015).

The geochemical composition of the pyroxenes includes subcalcic augite ($Fs_{20.8-21.8}Wo_{36.4-34.1}$), ferroan subcalcic augite ($Fs_{39.1}Wo_{30.7}$), pigeonite ($Fs_{33.7-53.1}Wo_{11.8-11.6}$), ferropigeonite rims ($Fs_{65.1-67.1}Wo_{18.7-14.4}$), ferrosilite ($Fs_{75.4}Wo_{2.0}$), maskelynite with plagioclasic composition ($An_{42.3-45.3}Or_{2.8-2.7}$) and anorthoclase ($An_{33.4}Or_{15.0}$) (Meteoritical Bulletin, 2014).

The validation of spectral data was carried out comparing the spectra with chemical analyses performed on the slab by means of SEM, equipped with EDS spectrometers. The choice of SEM as the validation technique was made with the aim of tracking the correspondence between spectral and chemical images. The results obtained contributed also to hypothesize the history of this meteorite: from the early igneous stage up to the final terrestrial contamination.

Experimental setup

VIS-IR reflectance spectroscopy

The shergottite slab (Fig.1) was analyzed by means of the SPectral IMaging (SPIM) facility (Fig.2a) and successively by Scanning Electron Microscopy (SEM). SPIM is a laboratory set-up that has been developed to support remote sensing observations of Solar System bodies (Coradini *et al.*, 2011; De Angelis *et al.*, 2015). It operates in a wide spectral range 0.2-5.1 μm and is characterized by high spatial (38 μm / pixel) and spectral (2 nm in the VIS channel, 12 nm in the IR channel) resolution. The target scan is performed by acquiring an image of the target along the slit, which is 9 mm long and 0.038 mm in width, and then moving the target in a perpendicular direction with respect to the slit by consecutive adjacent steps equal to the slit width. One spectrum corresponds to each single pixel along the slit (which in turn corresponds to 256 pixels in the VIS channel and 270 pixels in the IR channel). Therefore, a scan acquired on the target constitutes a 3-D data cube, with a 2-D image (Fig.2a) of the target and thousands of spectra in the third orthogonal dimension. The image size can be set in one direction and depends on the number of adjacent steps performed. For rocks with sub-mm surface heterogeneity (e.g. phenocrysts size) a typical image is in the range 9x5 to 9x10 mm^2. The reflectance calibration was obtained acquiring as reference target Spectralon Labsphere standards with reflectance values similar to the analyzed rocks (5-40%). For each spectrum the background measurement was performed by acquiring signal without illuminating the target, and it was subtracted from the measurement on the illuminated sample and the standard reference used. A straight line (1st order polynomial) joining the short-wavelength and long-wavelength edges of each single absorption band was used as continuum baseline; this baseline was then removed from the spectrum by division prior to analyzing the band. A 2nd order polynomial fit was instead used in order to reproduce the whole spectrum continuum baseline. RELAB and USGS spectral databases were used in order to allow the identification of spectral phases. The spectral wavelengths at about 1.5 and 2.5 μm were removed because the junctions of two filters are present in these spectral regions. These filters affect the spectra with artifacts that can be misleading (see De Sanctis *et al.*, 2011 for further details).
The stacking of SPIM images (VIS and IR) was done taking control points on the two images (VIS and IR) and linking them. The stacking of SPIM on SEM image was done taking control points on the two images and linking them. The spatial resolution of the SEM image of the whole slab was around 10 μm. Since the spatial resolution of SPIM image is around 38 μm, a spatial resampling of SEM image is necessary before stacking of the two images.
The spectral maps were obtained following this procedure: 1) spectral fitting with library data of augite and pigeonite resampled at SPIM spectral wavelengths; 2) then the purest pixels of augite and pigeonite of SPIM spectra were mapped on the slab image. The threshold chosen for the band centers was set between 0.95-0.97 and 2.0-2.10, for mapping the pigeonite and between 0.98-1.12 and 2.11-2.35 for augite.

Scanning Electron Microscopy

SEM investigations were carried out at DICATECh Department of Politecnico of Bari, Italy. The instrument used is a Zeiss Field Emission SEM SIGMA 300 VP that works in both high vacuum and variable pressure modes with a resolution of ~ 10 nm. It is equipped with secondary and backscattered electron detectors, an in-lens electron detector, and a cathodoluminescence (CL) detector. The chemical analyses are provided by a Bruker energy dispersive X-ray spectroscopy system (EDS) with dual silicon drift detectors; each of them shows an area of 60 mm^2 and a resolution of 123 eV at Mn Kα. In order to carry out the SEM analyses, the slab was coated by graphite. In order to provide topographic information about the surface, Secondary Electrons (SE) and Back Scattered Electrons (BSE) images were also acquired. Chemical formulas of minerals were calculated on the bases of their chemistry and structural type (Klein et al., 2008).

Results and Discussion

The analyzed meteorite fragment, Northwest Africa 8657 (NWA 8657), is about 4x10 mm^2 in size, with a thickness of about 2 mm. A surface area of approximately 3.8x9 mm was scanned, taking 100 acquisition-lines and moving at steps of 0.038 mm. In Fig.2a an RGB colour image of the scan is shown (R:0.70 μm, G:0.53 μm, B:0.44 μm) whereas the average spectrum of the slab is shown in Fig.2b. The average spectrum is characterized by a blue slope, a reflectance level around 0.15 at 0.55 μm and absorption bands at 0.9-1.02 μm, 1.25-1.3 μm, and near 2 μm. These absorptions are due to a variable Fe content in clinopyroxenes and to the occurrence of maskelynite. Moreover, the metal OH absorption occurs at 2.75 μm, the absorptions due to of CO_3 are visible in the range between 3.25-3.45 μm doublet and around 4.0 μm; the absorption at 3.25-3.45 μm can be also due to terrestrial organics contamination; the doublet visible at 4.25 μm is due to the presence of ambient CO_2 gas. The OH/H_2O band at 2.75-3 μm does not occur in all the phases/pixel, however it does occur in holes and tends to become stronger when moving toward the slab edges. The spatial distribution indicate that is very likely due to terrestrial water contamination.

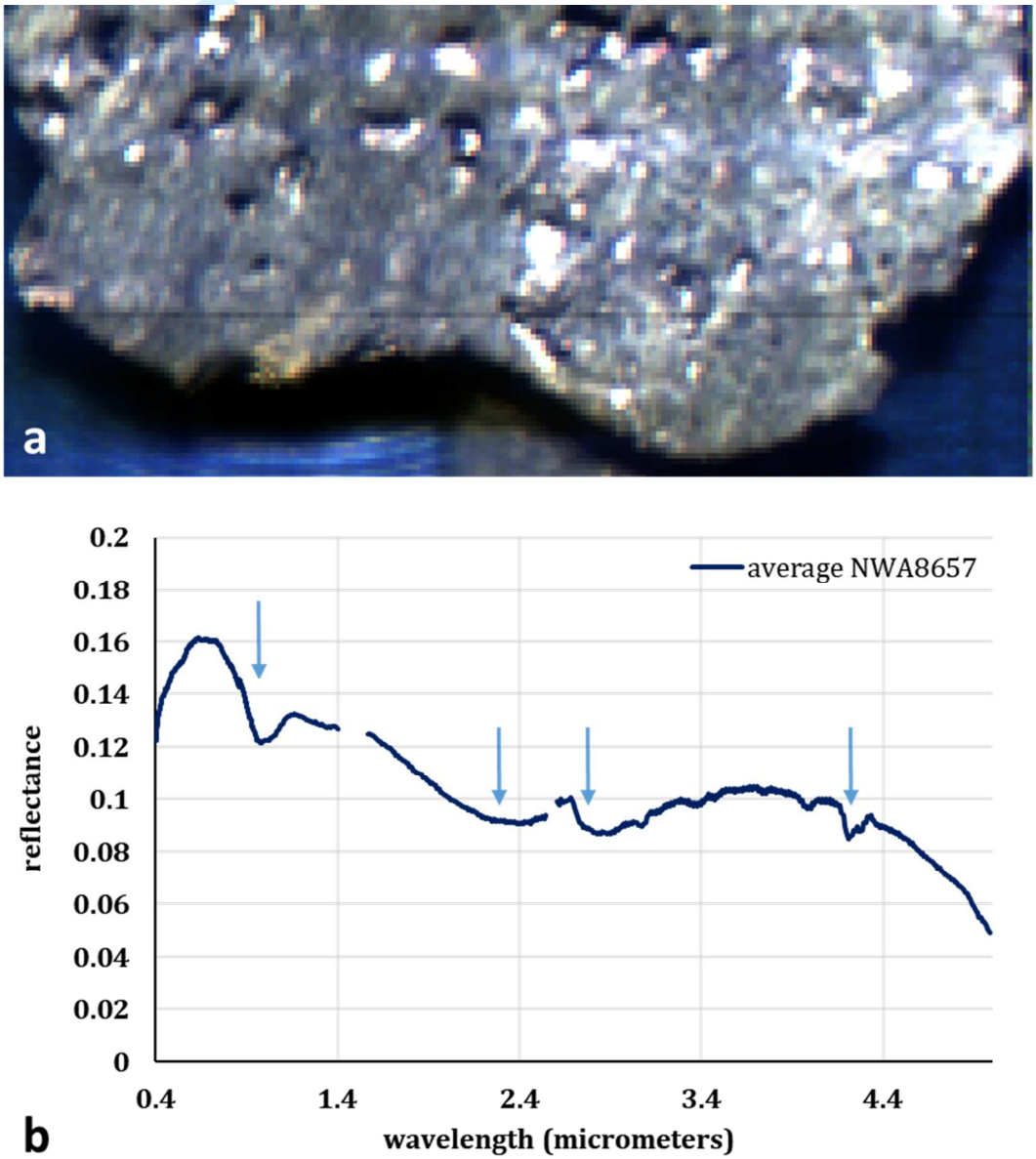

Fig.2. a) RGB (R:0.70 μm, G:0.53 μm, B:0.44 μm) image of NWA8657 shergottite acquired with SPIM; pixel size is 38 μm. b) Average spectrum of NWA8657 slab. Data around 1.5 and 2.5μm were removed because of instrumental artifacts

VIS-IR imaging spectroscopy analysis

The spectral investigations were done analyzing the slab pixel by pixel (38 μm), in order to ensure the validation by means of detailed comparisons between the spectral data and the SEM analyses. Most of the spectra, representing the main slab component, consist of reflectance spectra characterized by 1 and 2 μm features and in some cases a 1.2 μm feature. The reflectance is in the range 0.15-0.5. Previously, six main spectral classes were initially found by supervised classification before any comparison with SEM data (De Angelis *et al.*, 2016) including plagioclases, pyroxenes, Fe-Ti-oxides, a phase attributed in first instance to chromite/spinel and some traces of carbonate/carbonaceous and hydrous phases.
Here below, we describe the different spectra acquired on the sample, their distribution and their assignment to specific minerals.

Pyroxenes

Pyroxene spectra have reflectance values in the range 0.15-0.5 (Fig.3); they are characterized by differences in the band center positions and intensity of 1 and 2-μm features and in the positions of the shoulders at 0.85 and 1.2 μm. In some cases, spectra also show a 1.2-μm feature indicative of Fe- clinopyroxenes (Klima *et al.*, 2008; Adams, 1975).

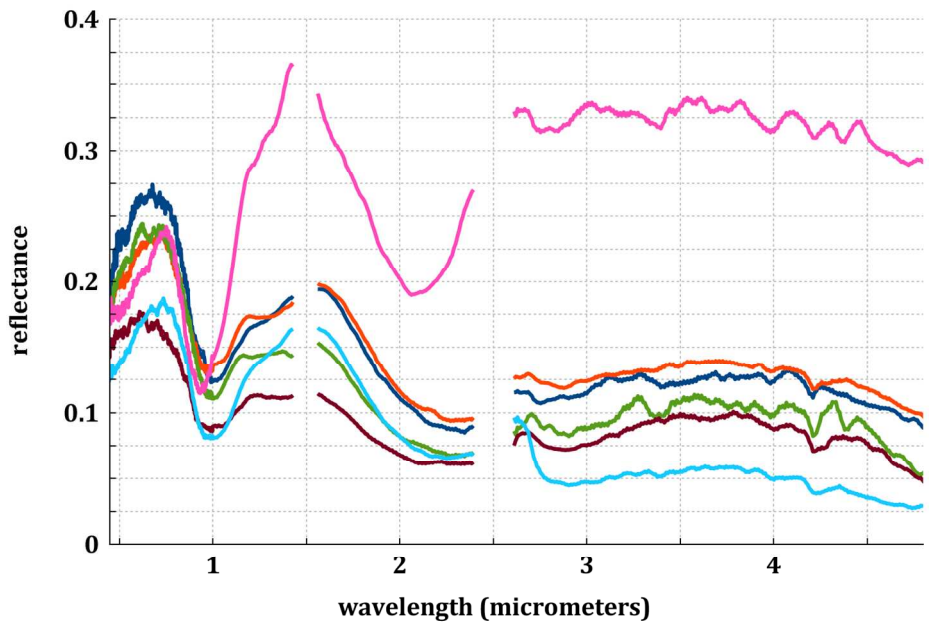

Fig.3. Variability of pyroxene-based spectra in NWA8657 slab. Each spectrum corresponds to a different pixel. Data around 1.5 and 2.5μm were removed because of instrumental artifacts.

In particular, the shoulder near 1.25-1.3 μm is affected by a shallow absorption that shows variable strength.
As demonstrated by Klima *et al.*, (2011) in low-Ca clinopyroxenes, the 1 μm band shifts regularly to longer wavelengths as a function of Ca^{2+} and Fe^{2+} as also the 2 μm band does. However, for content in Wo>30% the Ca^{2+} dependency of the 2 μm band position drops significantly because of the structural transition from pigeonite to augite.
The map in Fig.4a shows the purest pixels of pigeonite and augite absorptions (Fig.4b) on the slab SPIM image. The spectral variability of the pyroxenes in the slab can be observed in the 1 μm vs 2 μm plot in Fig.5, in which the band centers of each pixel associated to pyroxene were extracted after removing the continua.

Some pyroxenes spectra show the OH features at 2.75-3 μm and CO absorptions at 3.35-3.5 and 4 μm. These absorptions are due to subpixel mixing with carbonates and hydrated phases.

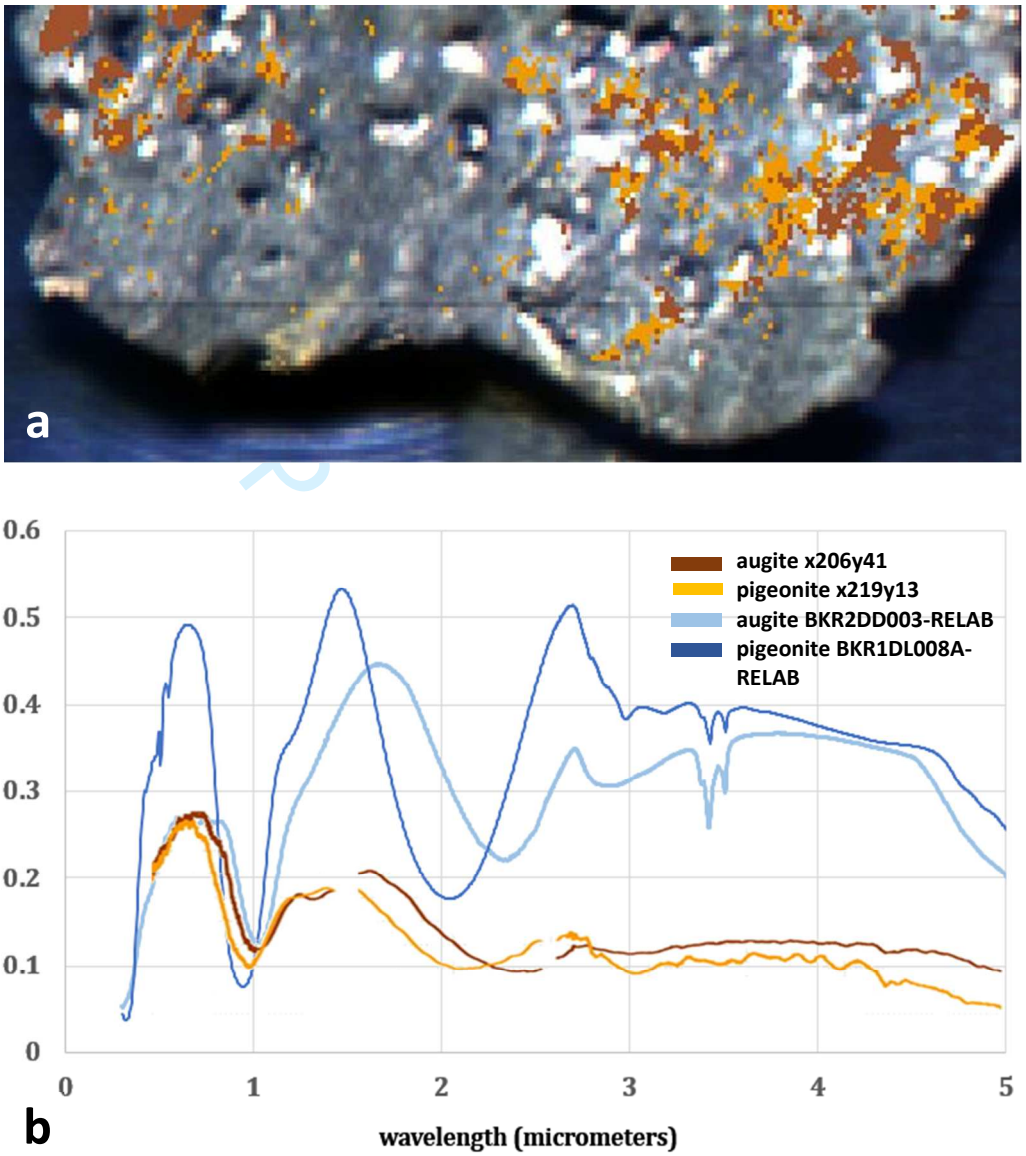

Fig.4. a) Map of augite (sienna), pigeonite (gold), absorptions on the RGB (R:0.70 μm, G:0.53 μm, B:0.44 μm) slab image; the procedure followed for the construction of the spectral map is described in the experimental section. b) Spectra of two pixels assigned to augite (coordinates of the pixel in the image: x206y41) and pigeonite (coordinates of the pixel in the image: x219y13) and comparison with augite and pigeonite from Relab library. Data around 1.5 and 2.5μm were removed because represent instrumental artifacts.

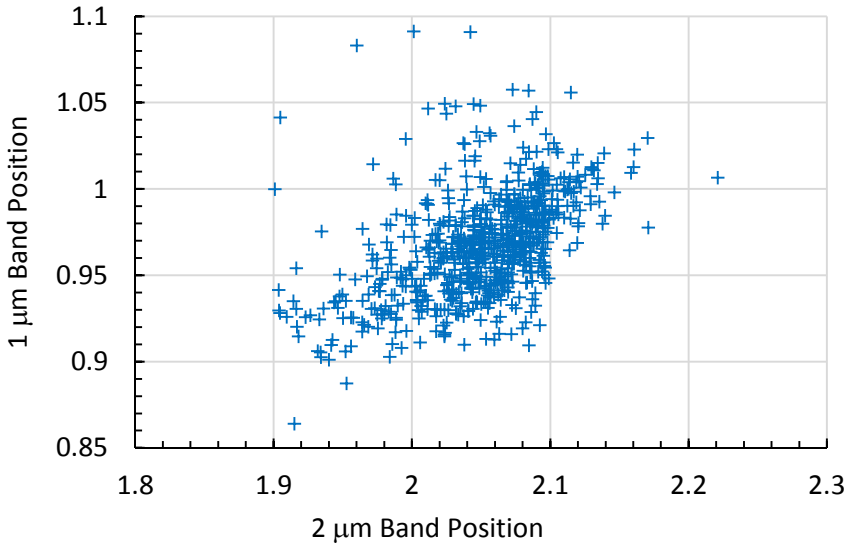

Fig.5. Pyroxene 1 µm versus 2 µm plot of pyroxenes in NWA8657 in this work. Each cross represents the absorptions related to the spectrum of each pixel associated to pyroxene.

Maskelynite

In this study, several spectra (Fig.6) with a blue slope and often a peak in the 0.6-0.7 µm, were found. These spectra occasionally show absorptions in the UV-VIS range and around 1 µm, that can be related to the contributions of other phases such as oxides or pyroxenes. As it can be seen in Fig.6a, these spectra have different features in commons with Relab library spectra of shocked plagioclase and maskelynite: the blue slope and lack of strong absorptions. The main differences stand on the reflectance values and the presence of H_2O features (1.4-1.9µm) in the maskelynite from Relab library. The blue slope is a well-known characteristic of the spectra taken on slab (Harloff and Arnolds, 2001; Pompilio *et al.*, 2007) and it is due to optical coupling. According to Hapke (1993), the optical coupling occurs when the surfaces of the particles are very close each other, within approximately a wavelength. In this case, the relative refractive indices across the grain boundaries are not from the mineral to air or to vacuum but from one mineral to another.

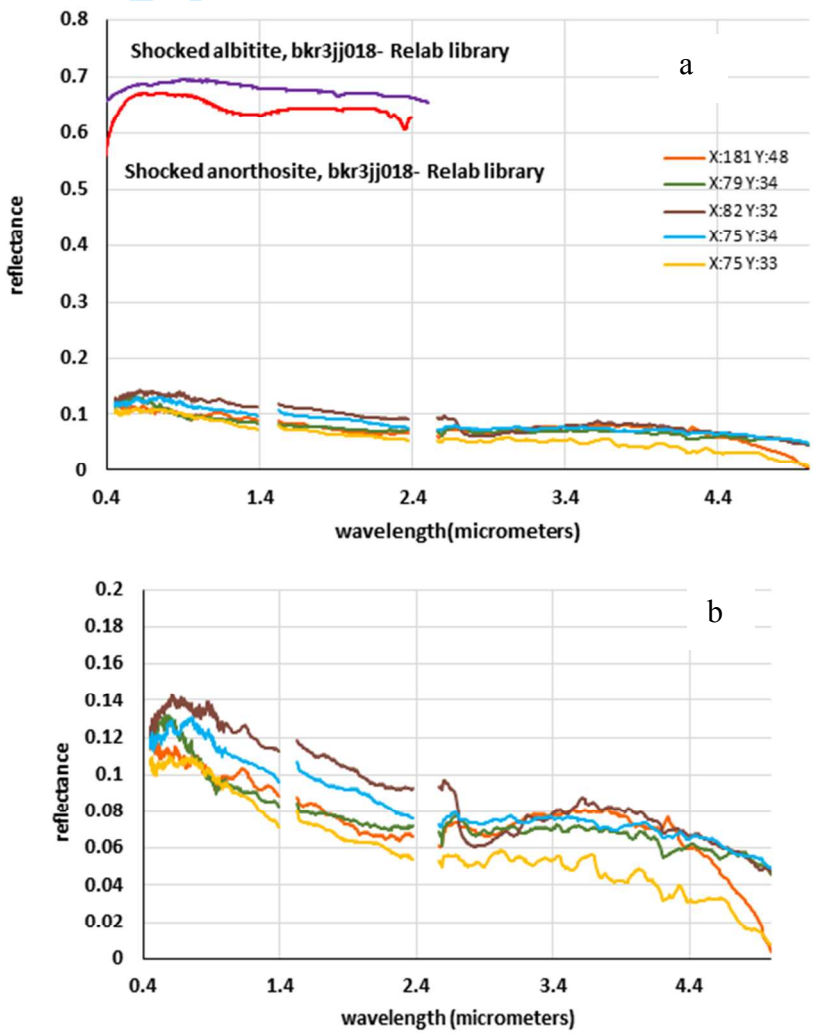

Fig.6. a) SPIM spectra of maskelynite grains in NWA8657 and comparison with shocked albitite and shocked anorthosite (Johnson and Horz, (2003. X and Y are the coordinates corresponding to the different pixels. Data around 1.5 and 2.5µm were removed because of instrumental artifacts; b) Zoom of the maskelynite spectra in Fig.6a

Fe-bearing opaque phases

The other major phases consist of spectra that lack a blue slope and show a broad absorption at 0.5 µm and sometimes weak absorptions near 0.9 µm (Fig.7). Moreover, these spectra show other minor absorptions. The spectra show a red slope and reflectance level below 0.2.

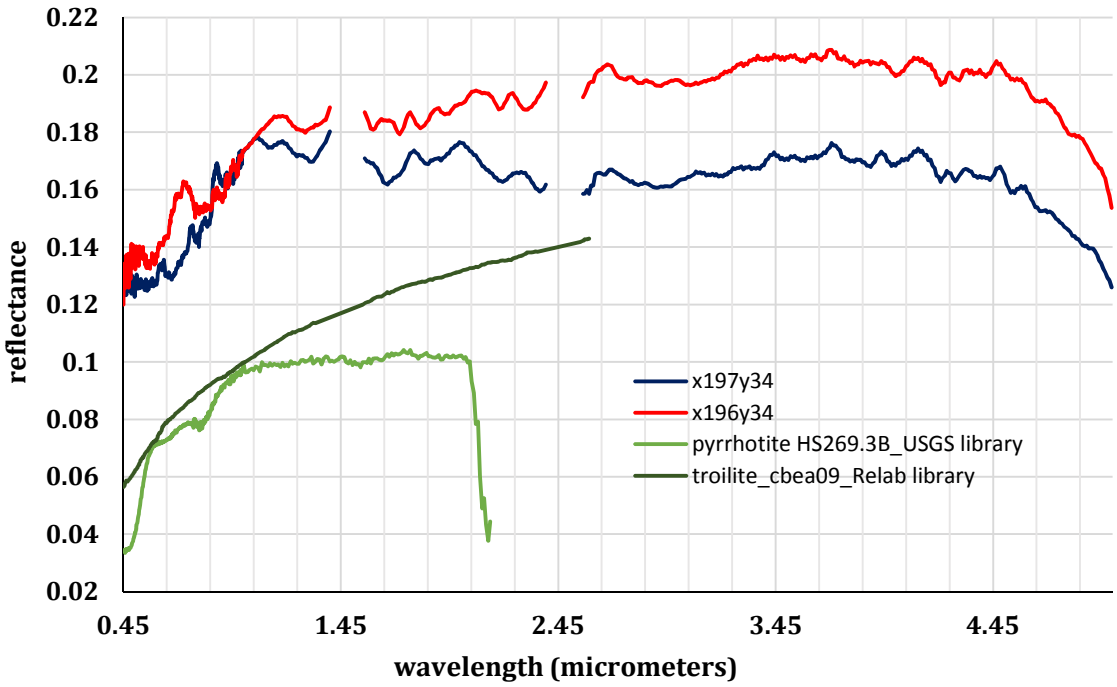

Fig.7. 0.5 µm and 1µm absorptions low-reflectance spectra in the NWA8657 slab. X and Y are the coordinates corresponding to the different pixels and comparison with pyrrothite and troilite from USGS and Relab libraries. Data around 1.5 and 2.5µm were removed because of instrumental artifacts.

Accessory phases: phosphates and carbonaceous phases

Two particular spectral families show minor absorptions in the 0.3-2.5 µm range and several more evident absorptions in the 2.75-3.5 µm region (Fig.8). All these spectra show the OH/H_2O band at 2.75-3 µm.

These two spectral families in the range 2.5-4 µm could be related to the presence of calcite and apatite. In fact, some pixels in the slab are characterized by strong absorptions in the region between 2.75 and 4 µm. Although apatite ($Ca_5(PO_4)_3(F,OH,Cl)$) should not show crystal field absorptions in the 0.3-2 µm range, and it shows the fundamentals transitions of X-$(PO_4)^{3-}$ and within $(PO_4)^{3-}$ ions in the 5-20 µm range (Jastrzebski *et al.*, 2011), this phase could produce OH-related vibrational absorptions in the 2-5 µm range. Indeed, we observe in some of our spectra (corresponding to SEM identifications of apatite) broad absorptions around 2.8 µm probably related to some OH/H_2O within apatite. The features near 3.5 and 4 µm could be assigned to apatite, which has an absorption at 3.47 µm and a doublet at 3.98 and 4.03 µm (Lane *et al.* 2007).

Other spectra show strong absorptions in the region around 3.25-3.45 µm and around 4.0 µm. These absorptions are typical of carbonates (Clark *et al.,* 2003, calcite ws272). However, not always the spectra show the features of carbonates at 2.35 and 2.5 µm (although the 2.5 µm feature must not be considered in SPIM spectra, because it overlaps with instrumental artifacts).

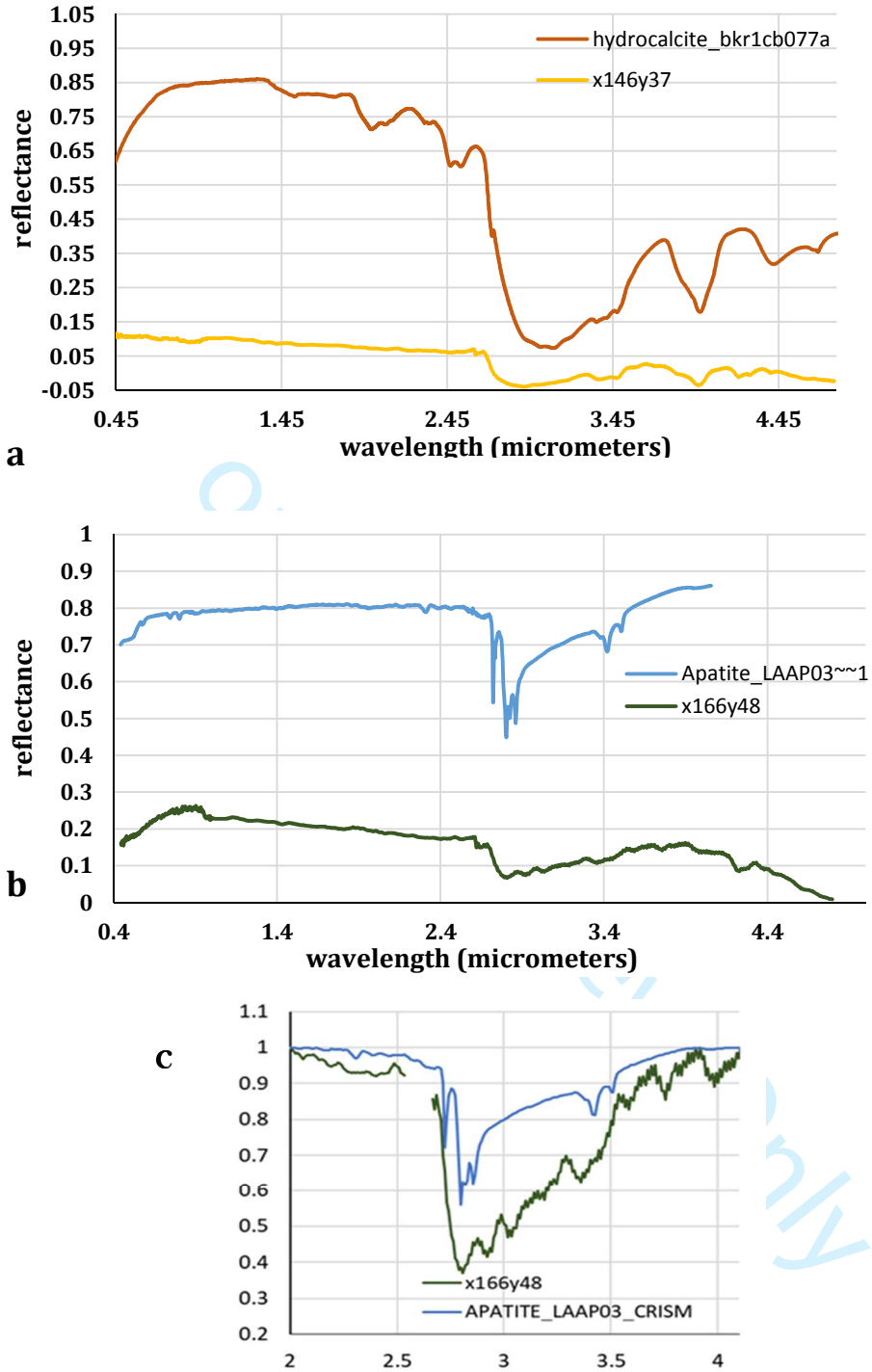

Fig.8a-b-c. a) Spectra of hydrated carbonates (146, 37) and hydrocalcite from Relab library. b) Spectra of phosphate phase (166,48) and apatite from CRISM library. X and Y are the coordinates corresponding to the different pixels. Data around 1.5 and 2.5µm were removed because of instrumental artifacts. c)Zoom of the continuum removed spectra in fig.8b in the range between 2 and 4.1µm

SEM analysis

In order to strengthen and to confirm the aforementioned interpretation of SPIM spectra, a Back-Scattered Electron (BSE) image of the whole slab was taken by SEM (Fig.9). This image shows that our sample has a complex symplectic texture. The sympletic microstructures consists of fine- to very-fine-grained intergrowths of at least two phases displaying vermicular or viscous textures (Spry, 2013) (see also Fig.12b). The mineral chemistry of the slab, obtained by Energy Dispersive X-Ray Spectroscopy (EDS) analyses and the derived chemical formula for the main phases are listed in table 1. The most abundant phase is pyroxene that is up to 300 µm in size and consists of Ca rich and Ca poor clinopyroxenes: augite $En_{4-40}Wo_{25-36}Fs_{24-64}$ and pigeonite $En_{40-70}Wo_{10-14}Fs_{20-43}$ (see Fig.10 and table 2). The chemical analyses performed on pyroxene show that each grain exhibits a complex chemical zoning with Mg-rich core and Fe-rich rim. The variability of the clinopyroxenes composition is well visible in the En-Fs-Wo ternary diagram in Fig.11. Maskelynite laths that are up to 500 µm in size have Na-Ca plagioclase composition. SiO_2 glass is also present.
The EDS analyses reveal that the opaque grains consist of iron oxides (ulvospinel) and iron monosulfides (troilite/pyrrhotite).

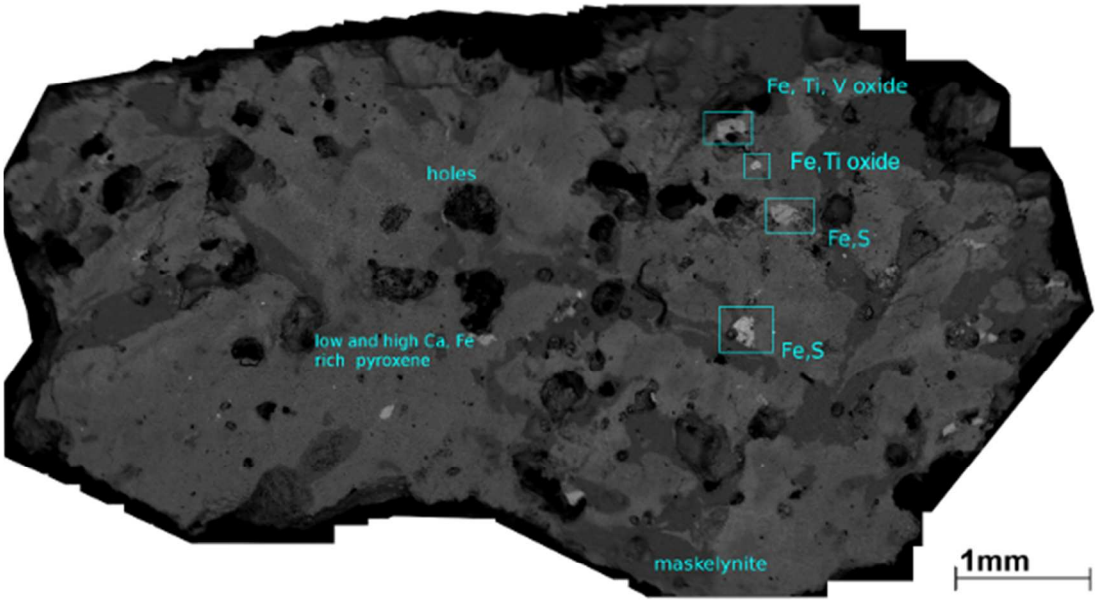

Fig.9. SEM-Backscattered image of slab NWA8657. The main phases found are indicated.

Table 1. List of the minerals detected by the SPIM spectrometer and the corresponding SEM-EDS analyses. Chemical formulas were calculated on the basis of the average composition for each mineralogical phase.

SPIM	SEM
Ca-rich clinopyroxenes	augite (Wo32% En37,97% Fs30,03%) $(Ca_{0.65}Mg_{0.26}Fe_{0.05}Mn_{0.02}Cr_{0.01}Ti_{0.01})$ $(Mg_{0.50}Fe_{0.50})$ $(Si_{0.94}Al_{0.06})$ O_6
Ca-poor clinopyroxenes	pigeonite (Wo18,50% En35,72% Fs45,78%) $(Ca_{0.35}Fe_{0.85}Mg_{0.70}Mn_{0.03}Al_{0.03}Ti_{0.02}Na_{0.02})(Si_{1.96}Al_{0.04})O_6$ $(Ca_{0.35}Fe_{0.85}Mg_{0.70}Mn_{0.03}Al_{0.03}Ti_{0.02}Na_{0.02})(Si_{1.96}Al_{0.04})O_6$
Maskelynite	Maskelynite glass (Albite 48.34%- Anorthite 50.21%-Orthoclase 1.45%)
opaque phases	Iron monosulfide $(Fe_{(1-x)}S)$, Oxides as Ulvospinel $(Ti_{0.61}Fe_{2.11}Si_{0.10}Al_{0.09}Mg_{0.03}Mn_{0.02}Cr_{0.02}V_{0.02})O_4$
hydrocalcite	calcite $(CaCO_3)$
phosphates	Fe-merrillite $(Ca_{9.29}Fe_{0.67}Mg_{0.54}Na_{0.25}Si_{0.20}Al_{0.18}(PO_4)_{6.87})$

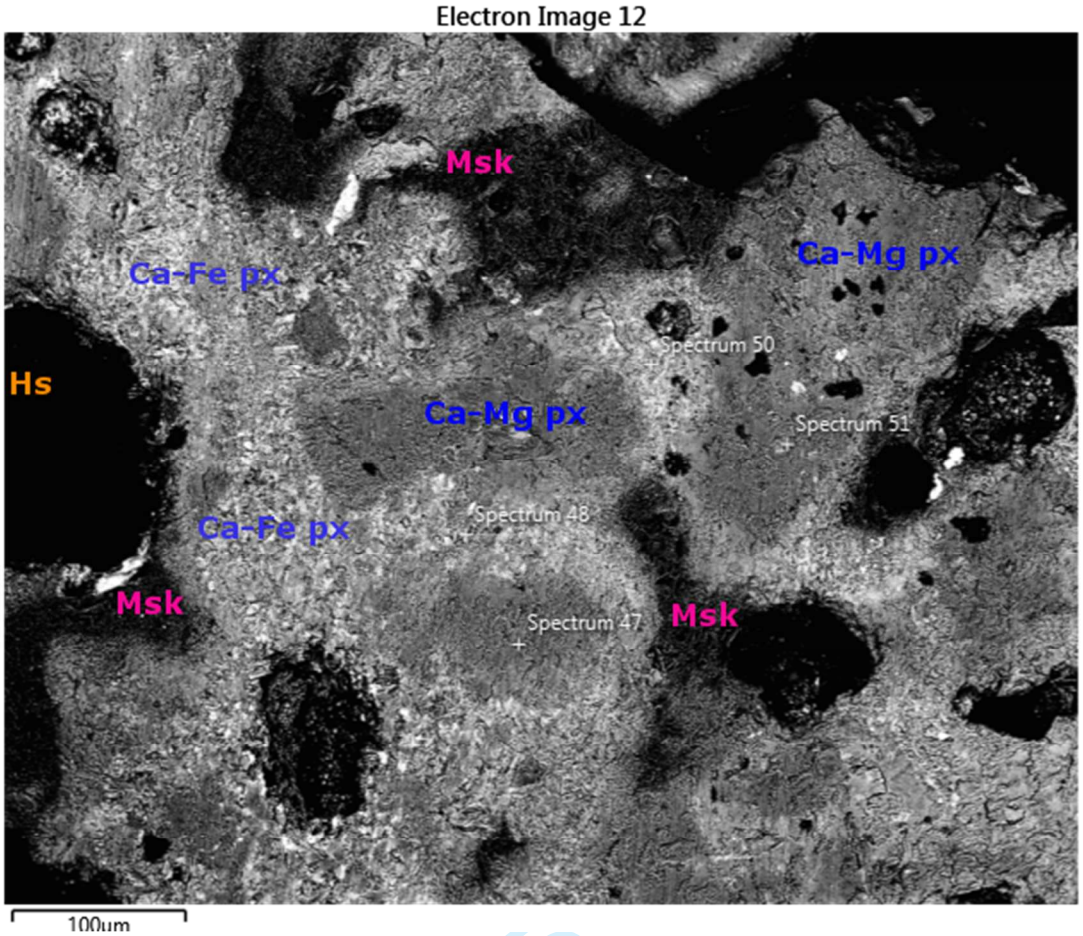

Fig.10. BSE image showing the different composition of clinopyroxenes and maskelynite. Ca-Mg px= Ca-Mg clinopyroxene; Ca-Fe px= Ca-Fe clinopyroxenes; Msk= maskelynite; Hs=holes. The composition of the spectra (47-48-50-51) on the BSE image are shown in table2.

Table 2. Quantitative data corresponding to the EDS punctual analyses acquired on the points marked on BSE image of Fig.10

% oxides	sp47	sp48	sp50	sp51
MgO	18.459	1.156	6.850	14.989
Al_2O_3	1.131	5.048	0.807	1.485
SiO_2	51.134	45.859	47.071	50.400
CaO	5.245	12.263	12.069	17.265
TiO_2	0.339	1.286	0.855	0.000
Cr_2O_3	0.314	0.000	0.000	0.696
MnO	0.904	0.723	0.841	0.508
FeO	22.732	30.498	29.693	13.913
Wo %	10.776	32.549	26.954	35.248
En %	52.769	4.268	21.287	42.580
Fs %	36.455	63.183	51.760	22.171

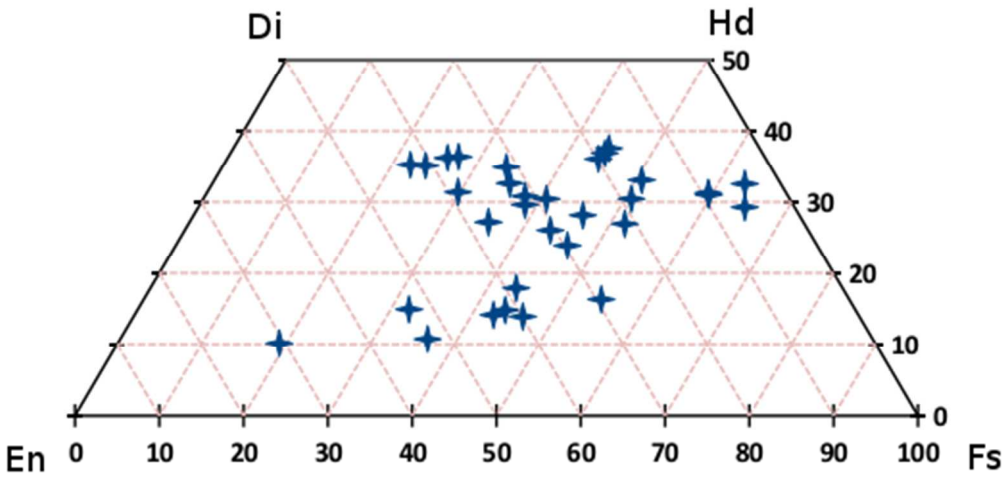

Fig.11. NWA8657 pyroxene compositions.

Interpretation of results comparing Spectral, SEM and literature data

North West Africa 8657 shergottite average spectrum

The average spectrum of the slab is shown in Fig.12 and is compared with previous spectral measurements on powders of Martian meteorites (McFadden and Cline, 2005). The different reflectance values represent both textural effects, powder versus slab, as well as the reflectance of different proportions of constituent phases present in different meteorites. In fact, the average spectrum of the slab shows a blue weak slope and a reflectance level around 0.15 and three main absorptions: at 0.95 μm, 1.25-1.3 μm and one beyond 2 μm. The different wavelength positions of the 1 and 2 μm absorption bands in different meteorite samples reflect the composition variability of the clinopyroxenes occurring in the slab.

The blue slope is generally observed on spectral profiles related to rock slabs and bulk rocks as reported by Harloff and Arnold (2001). These authors focused attention on the spectral differences in the NIR reflectance spectra of powders and bulk surfaces of pyroxenes and basalts as planetary surfaces analogs. Most of the powdered samples show a trend from positive to negative slope according to grain size, whereas nearly all specimens measured as a whole rock or slab had a blue slope. Furthermore, they studied the effects on the spectra of a variation of the roughness of the bulk surfaces. In this respect, they found that the brightness decreased exponentially with the increasing of the average grain size in the powdered specimens and of the mean roughness depth in the bulk specimens and the NIR slope increased with increasing grain size/mean roughness depth, reached a maximum, and then decreased.

In the case of the present work the spectral data were acquired by a high spatial resolution imaging spectrometer with respect to the aforementioned studies in which coarse resolution spectrometers were used to measure bulk data.

Recently, De Angelis *et al.*, (2014) studied the spectral properties of slabs viewed by means of the spectral imager Ma_MISS which has a spatial resolution of 120 μm. The spectral profiles at this spatial resolution do not display always a blue slope.

In the case of the present work, the observation that some pixels of the slab do not show blue slope leads us to think that the blue slope displayed in the average spectrum in Fig.12 could also indicates the presence of phases with a negative slope. In fact, analyzing the slab pixel by pixel, in those pixels corresponding to maskelynite amorphous/disordered phase the negative slope become more evident, also due to a peak in the visible range. This is in agreement with what was found by Manzari *et al.,* (2016) that studied two slabs of two Mars analogs by means of the SPIM imaging spectrometer. In those slabs, not all the pixel spectra were affected by a blue slope.

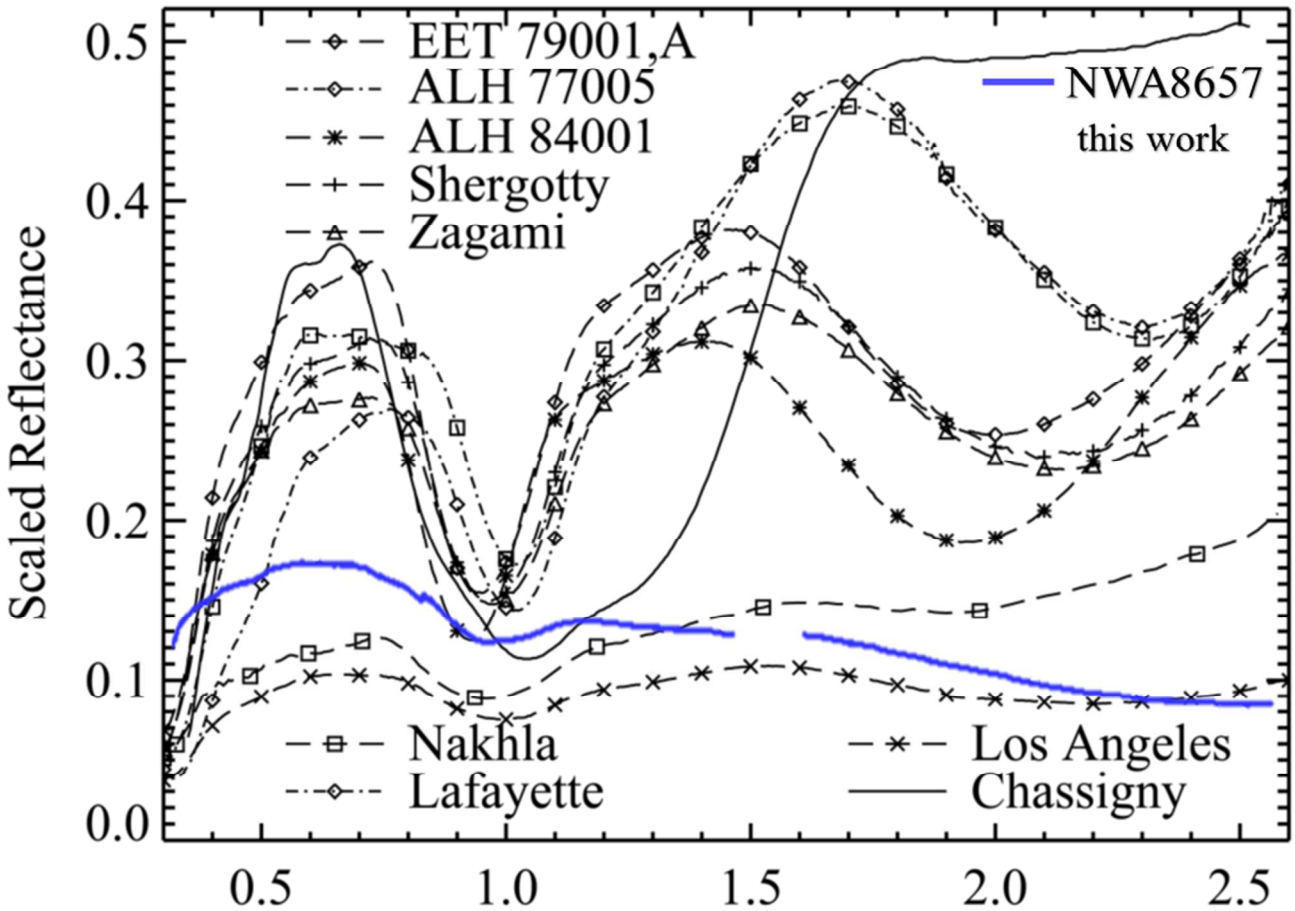

Fig.12. Modified after McFadden and Cline (2005). Comparison between spectral signatures of different Martian meteorites and North West Africa 8657 slab analyzed in this work.

Comparison with SEM

With the aim of improving the identification and interpretation of SPIM spectra, a SPIM image was linked to the SEM image through a co-alignment of some particular features that were recognizable in both the images: corners, holes, dips and microstructures. This procedure, called Ground Control Points (GCP) and borrowed from remote sensing data analyses, uses those morphological features for linking images. In this way the spectra of pixels near these spatial features can be linked to the corresponding EDS spectra, providing, for the first time, a good correlation between the two methods.

Thanks to GCP co-alignment of the two kinds of images (Fig.13), it was possible to cross check the major phases and their distribution with more confidence than in previous validation studies. However, two things must be considered: first, the two images have different spatial resolution: 38 μm x 38 μm for SPIM, while 2-10 μm for SEM image (Fig.13). Furthermore, the co-alignment of images is done on the basis of common morphological features (cracks, holes, edges) that are directly recognizable only in the visible range. The algorithm used allows checking for the common points, to calculate the Root Mean Square (RMS) error, and then to remove the GCPs with too high RMS error.

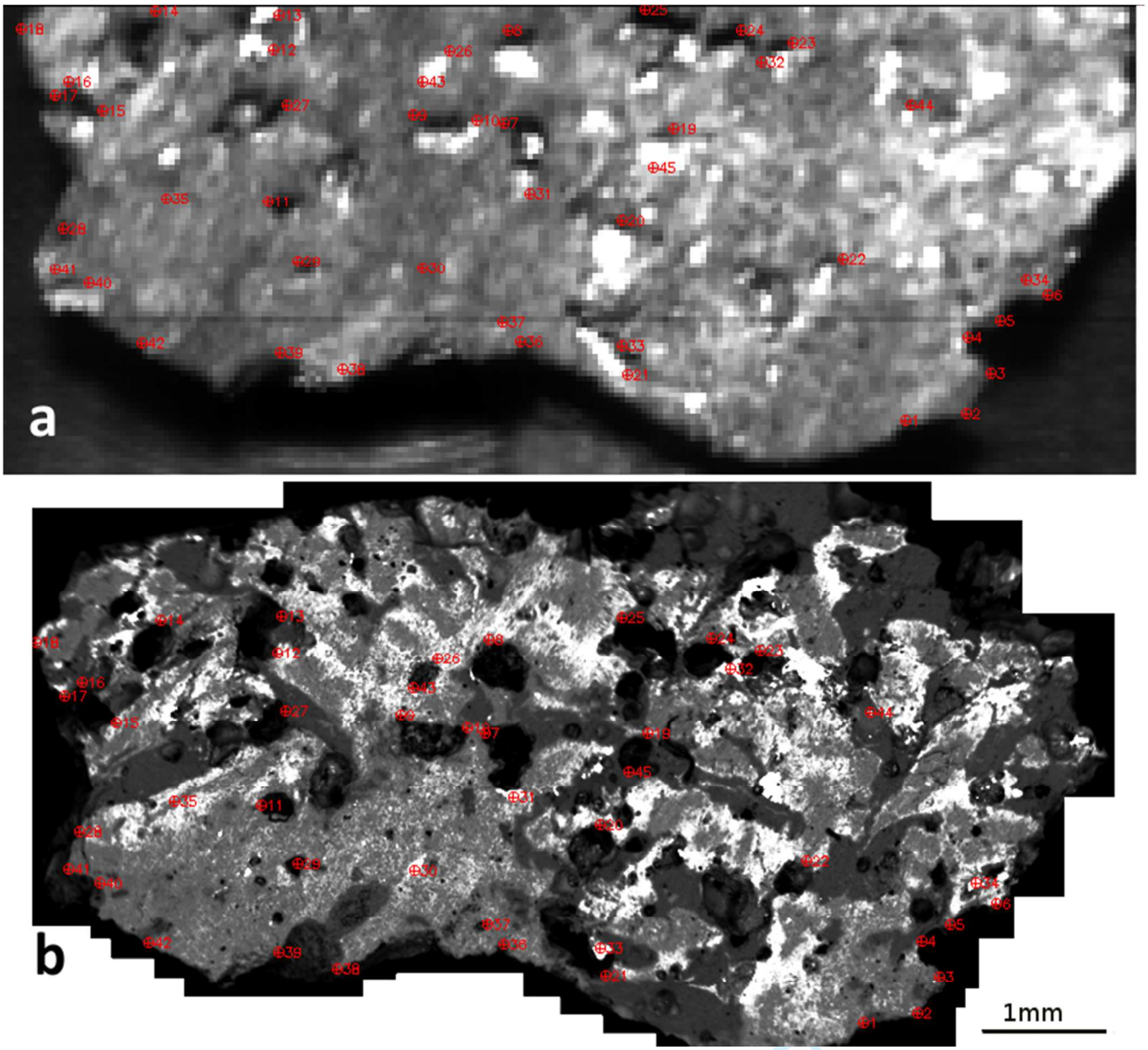

Fig.13. Co-alignment of SPIM image (a) and SEM-BSE image (b) *Red numbers correspond to the common features in the two images.*

Pyroxenes

This procedure was followed for pyroxenes. They form intergrowth microstructures too small to be determined by SPIM resolution. In this case the GCP procedure is useful for the interpretation of the main spectral class present in this slab, corresponding to a Fe-rich pigeonite; it affects the shoulder at 1.2-1.3 µm of the pyroxene and occurs mainly as intergrowth "worms" from Ca-rich pyroxene. The bands at 0.96 and 2.11 µm result from Fe^{2+} electronic transitions in distorted M2 sites. The band at 1.25 µm is due to Fe^{2+} in the crystallographic M1 site, typically in high-Ca pyroxenes or in quickly cooled disordered high-Fe pyroxenes in volcanic rocks (Klima *et al.*, 2008).

Data of this work show an overall composition between pigeonite and augite. Their chemical composition result in agreement with the predicted band positions for Ca rich and Ca poor pyroxenes in the quadrangles of Klima *et al.*, (2011) (Fig.14).

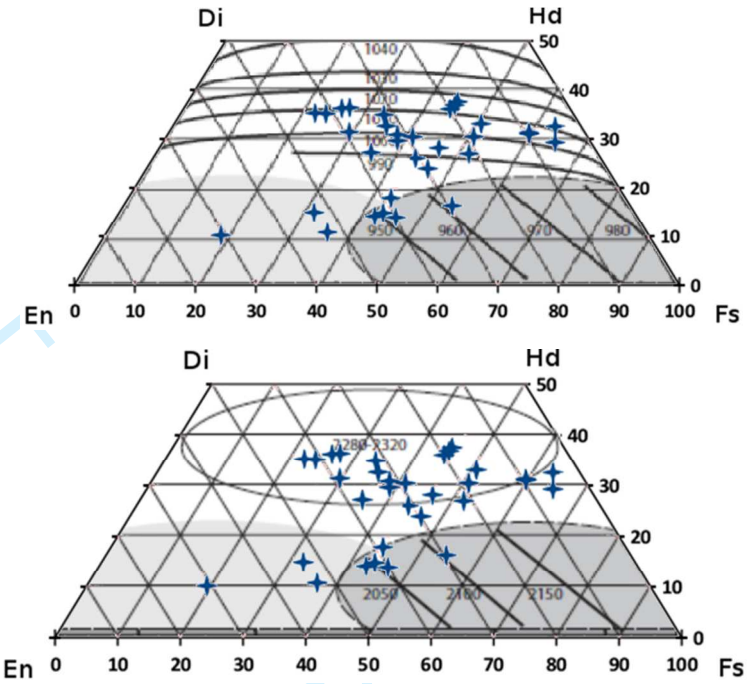

Fig.14. Plot of EDS representative compositions of the pyroxenes in this work (blue crosses) on the Klima et al., 2011 quadrangles of predicted positions of band absorptions for pyroxenes.

Clinopyroxenes in basaltic shergottites coprecipitated during crystallization of the parent magma, and since the Mg-rich pyroxenes exhibit a crystallization temperature higher than the Fe-rich ones, the solidification began with Mg-rich phases and continued with a progressive increasing of Fe, producing zoned pyroxenes. According to the pyroxene phase diagram (Lindsley 1983; Sack and Ghiorso 1994), crystallization started with Mg-rich pyroxene at temperatures between 1200 and 1100 °C and was completed after a cooling of about 50 °C with the formation of Fe-rich rims. The fact that the Fe-Mg zoning is not obliterated indicates a relatively fast cooling of the parent magma (Leroux *et al.*2004).

Nevertheless, in the sample studied in this work the clinopyroxenes occur both as single Fe/Mg weakly zoned crystals and as intergrowths/symplectic structures. In shergottites, the formation of symplectites is commonly attributed to a replacement of ferrosilite-rich pyroxene with a composition belonging to the 'forbidden' zone of the pyroxene quadrilateral (pyroxferroite) that can be formed by a cooling at 990 °C for over 3 days (Lindsley *et al.* 1972). The symplectites consist of grains, of about 1–10 μm in size, with the following mineralogical composition: fayalite + SiO_2 polymorphs, hedenbergite and merrillite $(Ca_9NaMg)(PO_4)_7$. Previous studies found that Mg is mainly bound to the merrillite and/or whitlockite $(Ca_9[Fe,Mg][PO_3OH][PO_4]_6)$structure, forcing the crystallizing pyroxene to extreme and unstable Fe-rich composition (Bridges and Warren and references therein, 2006).

Therefore, we infer the symplectites observed in the NWA8657 slab to be due to retrograde metamorphism that caused pyroxferroite to breakdown in Fe-rich more stable phases (Barker, 1998).

Maskelynite

In order to verify the presence of maskelynite, SPIM spectra of Fig.6 have been related to SEM analyses. An example is displayed in Fig.15: the spectrum of pixel x70y34 (Fig.15b) has the EDS composition of Fig.15d. Although the composition is plagioclase normative (Fig.15d) the phase is maskelynite, i.e. shock deformed plagioclase. Johnson and Horz, (2003), studying the visible and near-infrared spectra of experimentally shocked plagioclase feldspars, observed a complex behaviour in reflectance values of feldspars spectra at increasing shock pressures. However, on the basis of their experiments, the value of maskelynite reflectance in our work (<0.5) corresponds to shock pressures greater than 37 GPa. In this case, the low reflectance values would also be caused by intimate mixtures of small amounts of localized melts with vesicles and flow features and diaplectic glasses, which result in additional internal scatterers or discontinuities (Stoffler *et al.*, 1986; Yamaguchi and Sekine, 2000).

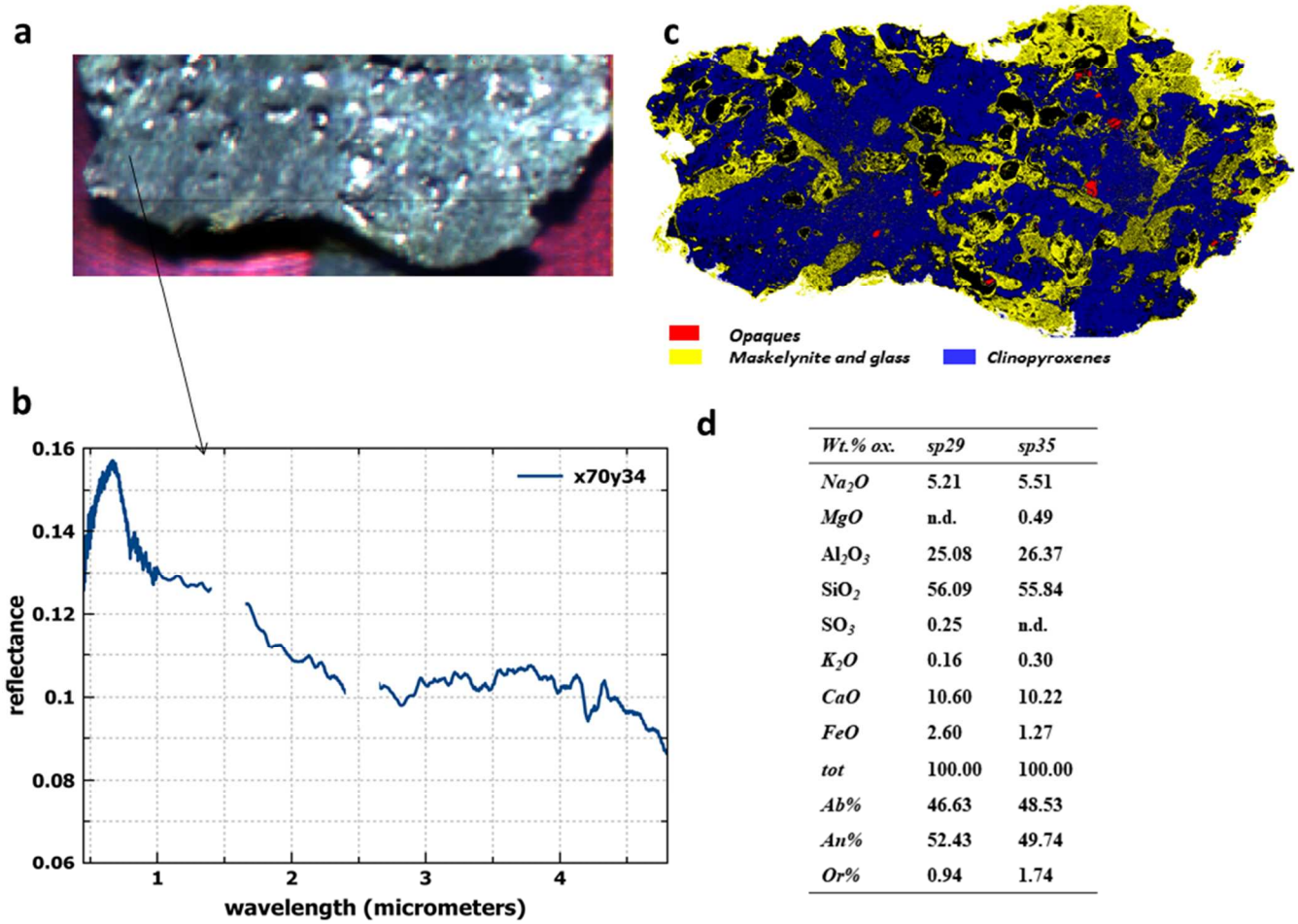

d

Wt.% ox.	*sp29*	*sp35*
Na_2O	5.21	5.51
MgO	n.d.	0.49
Al_2O_3	25.08	26.37
SiO_2	56.09	55.84
SO_3	0.25	n.d.
K_2O	0.16	0.30
CaO	10.60	10.22
FeO	2.60	1.27
tot	100.00	100.00
Ab%	46.63	48.53
An%	52.43	49.74
Or%	0.94	1.74

Fig 15. a) SPIM RGB (R:0.70 μm, G:0.53 μm, B:0.44 μm) image; b) arrow indicates the spectrum related to the pixel in a); c) false color map of the main components of the slab on the basis of EDS and BSE analyses: maskelynite-yellow; pyroxene-blue; opaque phases-red. d) EDS quantitative data related to some grains with maskelynite composition.

Troilite/pyrrhotite

In Fig.16, the spectrum of one of the two larger iron sulfide grains is shown. The grain, troilite/pyrrhotite, is about 100 to 200 μm in size, as assessed through SEM investigation. In the SPIM dataset, the 38 μm-resolution implies that each of these grains, consisting of pure iron mono-sulfide (FeS) is covered by at least two pixels. The corresponding spectra show an absorption feature in the range 0.47-0.6 μm, and an electronic transition absorption band near 0.9 μm, that are expected for iron sulfides and in agreement with that found by Cloutis and Burbine (1999), all attributable to ferrous iron transitions (Vaughan D.J. and Craig J.R., 1978). The exact mineralogical phase constituting these iron sulfide grains cannot be determined by SEM or VIS-NIR spectroscopy. However, Lorand *et al.*, (2005) analyzed the iron sulfides of four basaltic shergottites by X-Ray Diffraction (XRD) finding that their composition is mainly pyrrothite.

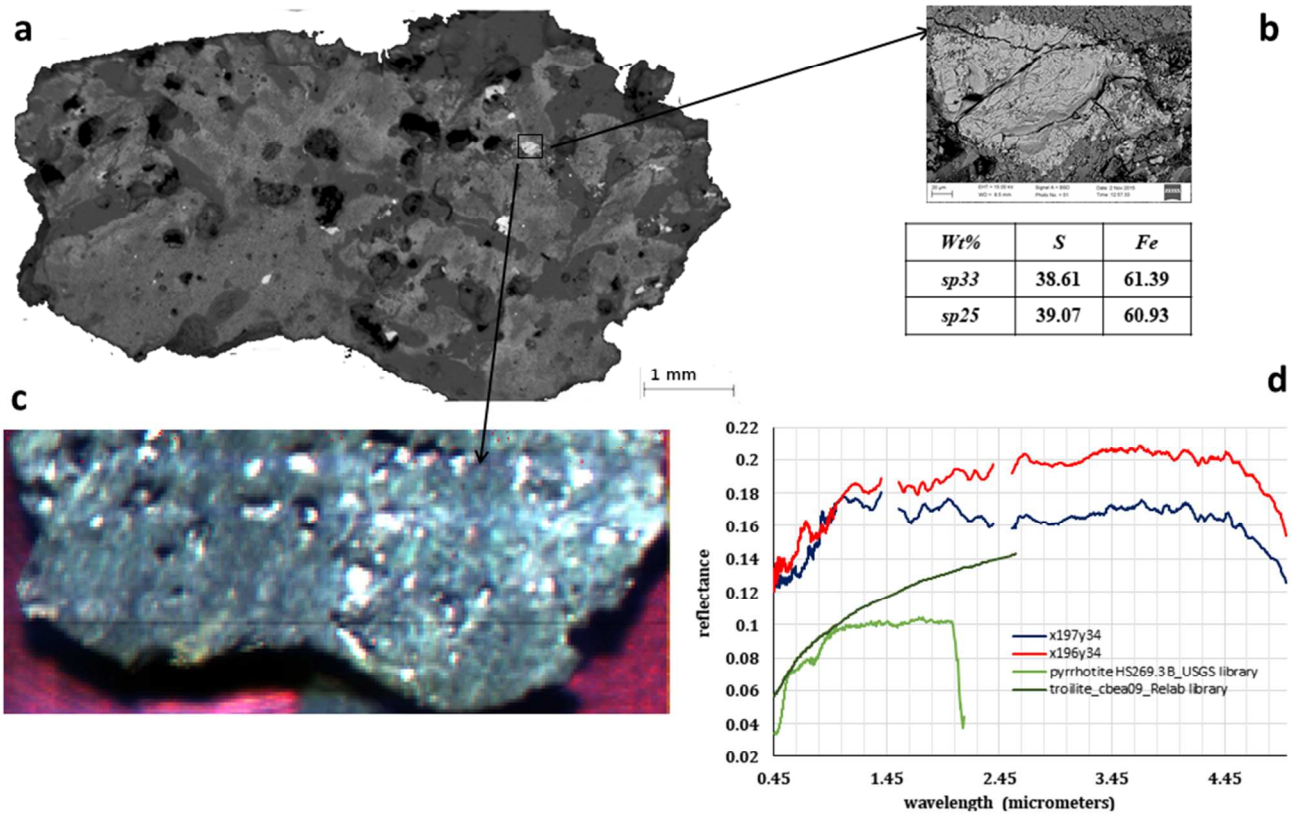

Fig.16. (a) BSE image by SEM showing white grains corresponding to troilite/pyrrhotite; (b) quantitative EDS data related to the troilite/pyrrhotite grain; (c) SPIM image: the arrow shows the pixel corresponding to the troilite/pyrrhotite grain; (d) Pixel spectrum (x196y34) in SPIM image and comparison with library spectra of troilite and pyrrhotite.

Ca-phosphates

Ca-phosphates such as merrillite and apatite were previously found in this meteorite by Hu *et al*., (2016). In this work, the occurrences and distribution of Ca-phosphate grains were inferred firstly from SPIM spectra before their identification in the slab by SEM. The 2.5-4.8-µm region was analyzed and both OH and CO_3 features apatite and calcite features were found that could putatively match with apatite and calcite phases, respectively. As previously stated in the results section, in fact, apatite does not display diagnostic absorption features in this spectral range; it only could be identified based on OH absorption occurring near 3 µm. In particular, SPIM data were compared with spectra of calcite and Cl-and F- apatite from RELAB and CRISM libraries according to the following approach: (i) SPIM spectra were resampled to the wavelengths of the library spectra, in the range between 2.2-4.8 µm, (ii) spectral features fitting was computed. Once the pixels showing best matches with features of apatite and calcite were found, the spectral fitting was used again to map these phases on the slab. For mapping the apatite on the slab, the 2.75-µm of OH absorption was used. This procedure served to make more rapid the location and determination of the composition of all of these isolated grains by SEM (Fig.17).
The phosphates previously ascribed to apatite by SPIM were analyzed also by EDS-SEM. The chemical analyses revealed a typical composition of Fe-merrillite [$Ca_9NaFe^{2+}(PO_4)_7$] which is the Fe^{2+} dominant endmember of merrillite (Britvin *et al.* 2016). However, merrillite, which is an anhydrous phase, was detected by EDS analyses in the same grains corresponding to SPIM pixels identified as Cl-apatite, including the OH feature. It must be noted that there are no literature data for reflectance of whitlockite and therefore what appears to be spectrally apatite could be also whitlockite. Therefore, the OH features could be due to the presence of OH/Cl-apatite plus merrillite phases (Gross *et al.*, 2013, McCubbin *et al.* 2014, 2016) or merrillite formed by partially shocked whitlockite (Adcock *et al.*, 2017). In fact, the slab showed other features that are characteristic of shock metamorphism e.g. maskelynite. The grain size of the phosphate is too small to reveal the co-presence of the two phases in the slab by SEM. Therefore, the Ca-phosphate found in our sample could be an intermediate phase belonging to merrillite ($Ca_9NaMg[PO_4]_7$)- whitlockite ($Ca_9[Fe,Mg][PO_3OH][PO_4]_6$) solid solution series (Hughes *et al.*, 2008), exhibiting a Fe-merrillite composition. This hypothesis explains the presence of the OH feature, not detectable by EDS-SEM analyses and confirms previous finding of merrillite in shergottite Martian meteorites (for example Ikeda *et al.*, 2006 and reference therein). Since commonly igneous phosphate minerals form in the late stages of magma evolution, including just before magma degassing to the surface (Shearer *et al.*, 2015) the volatile content and intergrowth relationships of phosphate minerals in Martian meteorites have been used as indicators of late-stage melt evolution. Thus, the pervasive occurrence and anhydrous nature of merrillite have been previously interpreted as evidence of relatively dry late-stage Martian melts (McCubbin *et al.*, 2014 and references therein).

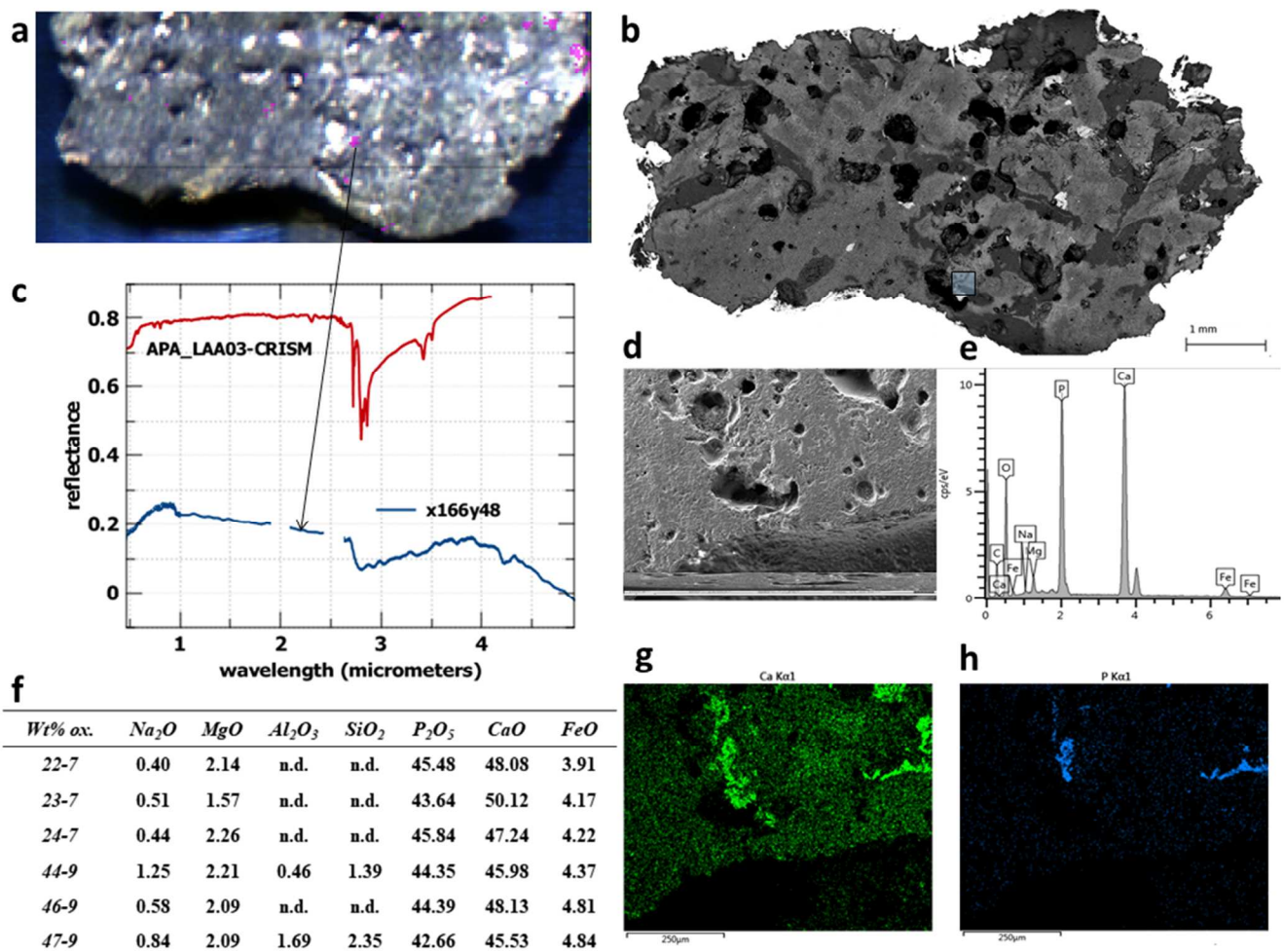

f

Wt% ox.	Na_2O	MgO	Al_2O_3	SiO_2	P_2O_5	CaO	FeO
22-7	0.40	2.14	n.d.	n.d.	45.48	48.08	3.91
23-7	0.51	1.57	n.d.	n.d.	43.64	50.12	4.17
24-7	0.44	2.26	n.d.	n.d.	45.84	47.24	4.22
44-9	1.25	2.21	0.46	1.39	44.35	45.98	4.37
46-9	0.58	2.09	n.d.	n.d.	44.39	48.13	4.81
47-9	0.84	2.09	1.69	2.35	42.66	45.53	4.84

Fig.17. a) Mapping of OH absorption assigned to the apatite (purple) on SPIM-RGB (R:0.70 µm, G:0.53 µm, B:0.44 µm) image and comparison with apatite spectrum named LAA03 from CRISM library. b) BSE-SEM image of NWA8657; framed area corresponds to the purple pixel in SPIM image; c) Spectrum of pixel x166y48; d) Secondary electron image of the enlarged detail selected in BSE image; e-f) EDS spectrum and EDS quantitative analyses; g-h) Ca and P of elemental maps of the same portion shown in (d) by EDS-SEM

Therefore, the coexistence of merrillite and apatite or whitlockite in the same meteorites have raised the question as to why merrillite rather than whitlockite forms in a melt with available H_2O at the time of phosphate crystallization (Hughes *et al.* 2008). Adcock *et al.*, (2017) tried to solve this question demonstrating that total/partial transformation from whitlockite to merrillite is possible by shock events. Consequently, in the case of the present slab, merrillite would be formed by shock events, whereas the hydrous phase was primary and directly related to latest igneous processes on Mars.

Calcite

Also, for Ca-carbonates grains the occurrence of calcite was inferred firstly from the observation of the SPIM spectra in the 2.5-4.8 µm region. Then the SPIM spectra were compared with spectra of calcite from RELAB and CRISM libraries according to the following approach: (i) SPIM spectra were resampled to the wavelengths of the library spectra, in the range between 2.2-4.8 µm, (ii) spectral features fitting was computed. Once the pixels showing best matching with features of calcite were found, the spectral fitting was used again to map the diagnostic features of calcite on the slab. Although calcite is often found in shergottites, for example in ALH84001 orthopyroxenite and Dhofar 019, is not clear whether it formed on Mars environment or not. Gooding and Muenow (1986a) and Gooding *et al.* (1988) found calcite (by XRD), an unspecified Ca-carbonate and low-Ca–carbonate (identified by SEM-EDS) in the shergottite EETA 79001 suggesting a pre-terrestrial Mars formation for them. In fact, some of these Ca-carbonates in the shergottite EETA 79001 occurred in veins and pockets of shock melt formed during an impact on Mars (Gooding *et al.* 1988), the same shock melt that trapped Martian atmospheric gases (Bogard and Johnson 1983). This suggests that at least these Ca-carbonate grains were already present in the rock when it experienced impact and shock on Mars, and they are carbonate grains of Martian origin (Gooding *et al.* 1988). However, calcite grains occur in holes and fractures within our sample (Fig.18), and this points to a likely terrestrial origin similarly to the case of Dhofar 019 (Taylor *et al.*2002). Furthermore, not all the carbonates spectra showed 2.35-2.55 µm bands. This effect could be caused by mixing of carbonates with low quantities of other secondary minerals such as quartz, smectite, sulfates as demonstrated by Mulder *et al.*, (2013).

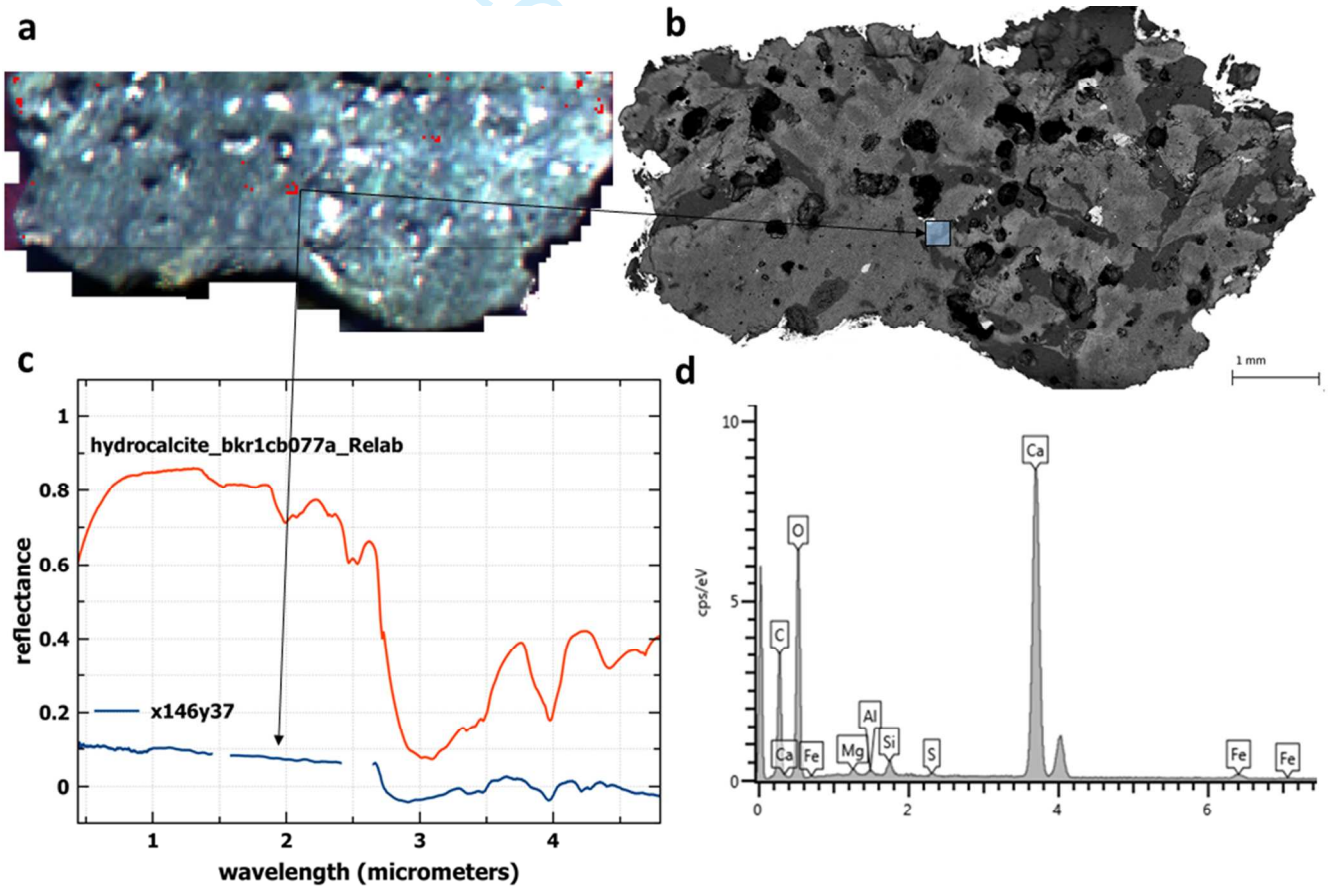

Fig.18. a) Mapping of hydrocalcite features (red) on SPIM-RGB (R:0.70 µm, G:0.53 µm, B:0.44 µm) image.; b) BSE-SEM image of NWA8657; framed area correspond to red pixel in SPIM image; c) Spectrum of pixel x146y37; d) EDS spectrum of calcite.

History of NWA8657 derived from spectral data and SEM analyses

The spectral results of this work allow us to hypothesize the history of this meteorite as follows:

1) Fe-rich clinopyroxenes and hydrous Ca-phosphates suggest an early igneous process.
2) The presence of amorphous phases as maskelynite proves shock by impact.
3) OH absorptions occurring on the edge and in the holes of the slab suggests terrestrial contamination.

The results obtained by SEM confirm those obtained by SPIM and add further elements. The chemical zoning of pyroxenes, the symplectitic texture and the finding of Fe-merrillite, suggest a new stage, with respect those hypothesized by SPIM investigations:

1) The presence of zoned pyroxenes (Mg-rich cores and Fe-rich rims) and whitlockite/apathite confirm an igneous origin for this meteorite.
2) symplectitic texture suggests breakdown of pyroxferroite
3) The presence of maskelynite and Fe-merrillite confirm that shock by impact occurred.
4) Terrestrial contamination by observing calcite in holes was also confirmed.

The reconstruction of the history of NWA8657 deduced by the integration of SPIM and SEM data can be summarized as follow:

1) igneous process in which Mg-pyroxene cores and progressive increasing of iron at rims, Na-Ca plagioclase, whitlockite and Cl-apatite formed;

2) retrograde metamorphism in which an intergrowth of microstructures from breakdown of pyroxferroite formed, in agreement with Hu *et al.* (2016);

3) shock by impact at pressures > 30GPa after crystallization, on the basis of the occurrence of large patches of maskelynite and grains of Fe-merrillite;

4) the fourth stage consists of the formation of secondary minerals such as calcite in holes and fractures by terrestrial weathering and sedimentary processes.

It can be concluded that a good agreement between SPIM and SEM data was found, even if these methods are characterized by different but complementary capabilities. In fact, the spatial resolution of SPIM does not allow to resolve the zonation of pyroxenes and the symplectites. On the other hand, the SEM EDS analyses do not allow to detect OH, well detectable by SPIM measurements.

Conclusions

The results obtained in this work allowed the analyses of the shergottite meteorite NWA8657 using the spectral data. Moreover, the validity of the high spatial resolution (at <40-μm scale) of VIS-IR imaging spectroscopy (0.4-5μm) for the identification of major mineralogical phases in rocks was validated by a detailed comparison with SEM analyses. In particular, comparisons between SPIM spectral data and SEM-BSE images by Ground Control Point procedure represent an innovative and valuable methodological approach to correctly interpret the data.

This kind of comparison is crucial to highlight the potentiality of SPIM to detect the main phases in a rock or a meteorite. The spectra univocally validated can be suitable for interpreting remotely sensed and in situ data that cannot be validated by other techniques.

The results of this work can be summarized:

- Spectral detection of the clinopyroxenes showing a composition from augite to Fe-rich pigeonite.
  SEM analyses on same grains verified the SPIM-detected compositional variation and revealed that these mineralogical phases are intermixed in form of intergrowths microstructures of Fe-pigeonite and silica phases down to 40 μm in size.
- Possible presence of maskelynite and glass patches on the basis of spectra with no or weak absorptions and blue slope. The spectral identification was done by the comparison with library spectra of shocked plagioclases and maskelynite.
  SEM analyses on same grains showed a variable composition of the original plagioclase, now maskelynite.
- Spectral detection of Ca-carbonate and Ca-phosphates in few isolated and concentrated regions of few pixels. By SEM analyses: calcite grains appear to be concentrated in holes. The analyses by EDS of Ca-phosphate grains that were interpreted spectrally as apatite showed a composition of Fe-merrillite/whitlockite.
- Spectral characterization of opaque Fe-bearing phases by detection of features in the range 0.47-0.6, near 1 μm and positive slope. The spectral identification was confirmed by the comparison with library spectra of iron sulfides. These phases consisted of iron oxides (ulvospinel) and troilite/pyrrhotite as inferred by EDS analyses.

Moreover, different spectral mineral components detected by SPIM can be isolated, thanks to the high spatial resolution, by spectral feature mapping and once validated the chemical/mineralogical composition, these can be part of a spectral library relative to a particular meteorite sample, or meteorite group. In fact, some of the mineralogical phases found on planetary surfaces or in meteorites are very rare and sometimes, as for the case of merrillite, need to be synthetized for creation of spectral libraries. This work also demonstrates that, while preserving the microstructures and the original mineral association, imaging spectroscopy could be used for the reconstruction of the rocks' histories and helpful in order to improve the mixing models for planetary measurements *in situ* and by remote sensing. In particular, in view of the ExoMars 2020 mission (Vago *et al*., 2017) this kind of spectral measurement on minerals characterized by the same paragenesis or same metamorphic/sedimentary processes, will aid the interpretation of data collected *in situ* by Ma_Miss (De Sanctis *et al.*, 2017) spectrometer.

Acknowledgements

The authors thank the Italian Space Agency (ASI) through grant n. 2015-002-809 R.0.

References

Adams, J. B., Interpretation of visible and near-infrared diffuse reflectance spectra of pyroxenes and other rock-forming minerals, in Infrared and Raman Spectroscopy of Lunar and Terrestrial Minerals, (1975) edited by C. Karr Jr., pp. 91–116, Academic, San Diego, California.

Adcock C.T., Tschauner O., Hausrath E.M., Udry A., Luo S.N., Cai Y., Ren M., Lanzirotti A., Newville M., Kunz M., Lin C. (2017) Shock-transformation of whitlockite to merrillite and the implications for meteoritic phosphate; Nature Communications, 8:14667, doi: 10.1038/ncomms14667.

Barker, A.J., (1998) Introduction to metamorphic textures and microstructures. Stanley Thornes Ltd., Cheltenham.

Bogard D.D. and Johnson P., (1983) Martian Gases in an Antarctic Meteorite? Science, 221, 651– 654.

Bogard, D.D., Nyquist, L.E., Johnson, P., (1984) Noble gas contents of shergottites and implications for the Martian origins of the SNC meteorites. Geochimica et Cosmochimica Acta 48, 1723–1739.

Bridges, J.C., and Warren, P.H. (2006) The SNC meteorites: Basaltic igneous processes on Mars. Journal of the Geological Society of London, 163, 229–251.

Britvin, S.N., S.V. Krivovichev, and T. Armbruster (2016) Ferromerrillite, $Ca_9NaFe^{2+}(PO_4)_7$, a new mineral from the Martian meteorites, and some insights into merrillite-tuite transformation in shergottites. European Journal of Mineralogy, 28, 125-136.

Cannon, K.M., Mustard, J.F., and Agee, C.B., (2015a), Evidence for a widespread basaltic breccia component in the martian low-albedo regions from the reflectance spectrum of Northwest Africa 7034: Icarus, v. 252, p. 150–153, doi: 10.1016/j.icarus.2015.01.016.

Clark R. N., Swayzen G. A., Wise R., Livo K. E., Hoefen T. M., Kokaly R. F., and Sutley S. J., (2003) USGS Digital Spectral Library splib05a, U.S. Geological Survey.

Cloutis E. A. and Burbine T. H. (1999) The Spectral Properties of Troilite/Pyrrhotite and Implications for the E-Asteroids; 30th Annual Lunar and Planetary Science Conference, abstract no. 1875.

Coradini, A., Piccioni G., Amici S., Bianchi R., Capaccioni F., Capria M.T., De Sanctis M.C., Di Lellis A.M., Espinasse S.,Federico C., Fonti S., Arnold G., Atreya S.K., Owen T. , Blecka M., Bini A.,Cosi M., Pieri S., Tacconi M. et al., (2001), MA_MISS: Mars multispectral imager for subsurface studies, Advances in Space Research, 28-8, p.1203-08.

Coradini, A., Ammannito E., Boccaccini A., Di Iorio T., Baldetti P. , Capaccioni F. , De Sanctis M.C., Filacchione G., Farina M., Bini A., Barbis A., Tarchi F. et al. (2011), Laboratory measurements in support of the DAWN mission: The SPectral IMaging (SPIM) facility, European Planetary Science Congress abstracts, vol. 6, 1043.

De Angelis S., De Sanctis M. C., Ammannito E., Di Iorio T., Carli C., Frigeri A., Capria M.T., Federico C., Boccaccini A., Capaccioni F., Giardino M., Cerroni P., Palomba E., and Piccioni G. (2014) VNIR spectroscopy of Mars Analogues with the ExoMars-Ma Miss instrument, Memorie della Società Astronomica Italiana, Vol. 26, 121.

De Angelis S., Manzari P., De Sanctis M.C., Ammannito E., Di Iorio T. , (2015), The spectral imaging facility:

Setup characterization, Review of Scientific Instruments, 86(9), 1–15.

De Angelis S., Manzari P., De Sanctis M.C., Ammannito E., Di Iorio T., (2016), Hyperspectral micro-imaging of Martian Shergottite Northwest Africa 8657 fragment in the Visible-Infrared range, 47th Lunar and Planetary Science Conference, abstract n.1223.

De Sanctis M.C., F. Altieri, E. Ammannito, D. Biondi, S. De Angelis, M. Meini, G. Mondello, S. Novi, R. Paolinetti, M. Soldani, R. Mugnuolo, S. Pirrotta, J. L. Vago and the Ma_MISS team, Ma_MISS On Exomars: Mineralogical Characterization Of The Martian Subsurface, Astrobiology, Volume 17, Numbers 6 and 7, DOI: 10.1089/ast.2016.1541, 2017

Ehlmann B.L., Blaney D.L., Green R.O., Mouroulis P., (2016), Vswir Microimaging Spectroscopy For Geologic History And Identifying And Quantifying Mineral, Ice, And Organic Abundances On Planetary Surfaces- 3rd International Workshop on Instrumentation for Planetary Missions.

Gooding JL, Muenow DW. (1986) Martian volatiles in shergottite EETA 79001: New evidence from oxidized sulfur and sulfur-rich aluminosilicates, Geochimica et Cosmochimica Acta 50:1049–1059.

Gooding JL,Wentworth SJ, Zolensky ME. (1988) Calcium carbonate and sulfate of possible extraterrestrial origin in the EETA 79001 meteorite. Geochimica et Cosmochimica Acta 52:909–915.

Greenberger RN, Mustard JF, Ehlmann BL, Blaney DL, Cloutis EA, (2015), Imaging spectroscopy of geological samples and outcrops: Novel insights from microns to meters, GSA Today 25 (12), 4-10.

Gross, J., Filiberto, J. & Bell, A. S., (2013), Water in the Martian interior: evidence for terrestrial MORB mantle-like volatile contents from hydroxyl-rich apatite in olivine–phyric shergottite NWA 6234. Earth and Planetary Science Letters, 369, 120–128.

Hapke, B. (1993), Theory of Reflectance and Emittance Spectroscopy, Cambridge Univ. Press, Cambridge, U. K. Harloff, J., and G. Arnold (2001), Near-infrared reflectance spectroscopy of bulk analog materials for planetary crust, Planetary and Space Science, 49, 191– 211.

Hiroi, T., Kaiden, H., Misawa, K., Niihara, T., Kojima, H., Sasaki, S., (2011), Visible and near-infrared spectral survey of Martian meteorites stored at the National Institute of polar research. Polar Science, 5, 337-344.

Hu S., Lin Y. T. and Zhang T., (2016) Petrography, Mineral Chemistry and Shock Metamorphism of Martian Meteorite NWA 8657, 79th Annual Meeting of the Meteoritical Society, abs#6068.

Hughes, J. M., Jolliff, B. L. & Rakovan, J. (2008) The crystal chemistry of whitlockite and merrillite and the dehydrogenation of whitlockite to merrillite. American Mineralogist 93, 1300–1305.

Ikeda Y., Kimura M., Takeda Hiroshi, Shimoda G., Kita N.T., Morishita Y., Suzuki A., Jagoutz Emil and Dreibus G. (2006) Petrology of a new basaltic Shergottite: Dhofar 378, Antarctic Meteorite Research, 19, 20-44.

Jaret, S. J., W. R. Woerner, B. L. Phillips, L. Ehm, H. Nekvasil, S. P. Wright, and T. D. Glotch (2015), Maskelynite formation via solid-state transformation: Evidence of infrared and X-ray anisotropy, J. Geophys. Res. Planets, 120, 570–587, doi:10.1002/2014JE004764.

Jastrzebski W., Sitarz M., Rokita M., Bulat K., (2011), Infrared spectroscopy of different phosphates structures, Spectrochimica Acta Part A: Molecular and Biomolecular Spectroscopy, 79, 722-727.

Johnson J.R. and Horz F. (2003) Visible/near-infrared spectra of experimentally shocked plagioclase feldspars Journal of Geophysical Research, Vol. 108, No. E11, 5120, Doi:10.1029/2003je002127

Klein, C., Dutrow, B., & Dana, J. D. (2008). *The 23rd edition of the manual of mineral science: (after James D. Dana)* (23rd ed.). Hoboken, N.J.: J. Wiley.

Klima R.L., Pieters C.M., Dyar M.D. (2008), Characterization of the 1.2 μm M1 pyroxene band: Extracting cooling history from near-IR spectra of pyroxenes and pyroxene-dominated rocks, Meteoritics & Planetary Science 43, Nr 10, 1591–1604.

Klima R.L., Dyar M.D. Pieters C.M., (2011), Near-infrared spectra of clinopyroxenes: Effects of calcium content and crystal structure, Meteoritics & Planetary Science, 46, Nr 3, 379–395.

Lane M. D., Dyar M. D., and Bishop J. L., (2007), Spectra of phosphate minerals as obtained by visible-near infrared reflectance, thermal infrared emission, and Mössbauer laboratory analyses. Lunar and Planetary Science XXXVIII, 2210.

Leroux H., Devouard B., Cordier P., Guyot F., (2004), Pyroxene microstructure in the Northwest Africa 856 Martian meteorite, Meteoritics & Planetary Science 39, Nr 5, 711–722.

Lindsley D. H., Papike J. J., and Bence A. E. 1972. Pyroxferroite: Breakdown at low pressure and high temperature (abstract). 3rd Lunar Science Conference. pp. 483–485.

Lindsley D. H. 1983. Pyroxene thermometry. American Mineralogist 68:477–493.

Lorand, J.P., Chevrier V., Sautter V. (2005), Sulfide mineralogy and redox conditions in some shergottites. Meteoritics & Planetary Science 40, Nr 8, 1257–1272

McCubbin F. M., Shearer, C. K., Burger P. V., Hauri E.H., Wang J., Elardo S., Papike J. J. (2014) Volatile abundances of coexisting merrillite and apatite in the Martian meteorite Shergotty: implications for merrillite in hydrous magmas. American Mineralogist 99, 1347–1354.

McCubbin, F. M., Boyce, J. W.; Srinivasan, P.; Santos, A. R.; Elardo, S. M.; Filiberto, J.; Steele, A.; Shearer, C. K. (2016) Heterogeneous distribution of H_2O in the Martian interior: implications for the abundance of H_2O in depleted and enriched mantle sources. Meteoritics & Planetary Science 51, 2036–2060.

Manzari, P., De Angelis S., De Sanctis M. C., Di Iorio T., E. Ammannito, N. Bost, F. Foucher, and F. Westall, (2016), Microimaging VIS-IR spectroscopy of ancient volcanic rocks as Mars analogues, Earth and Space Science, 3, 268–281.

McFadden L.A. and Cline T.P., (2005), Spectral reflectance of Martian meteorites: Spectral signatures as a template for locating source region on Mars, Meteoritics & Planetary Science 40, Nr 2, 151–172.

McSween Jr., H.Y., (1985). SNC meteorites: Clues to Martian petrologic evolution? Reviews of Geophysics, 23, 391-416.

McSween Jr., H.Y., (2002). The rocks of Mars, from far and near. Meteoritics & Planetary Science 37, 7–25.

Meteoritical Bulletin, (2014), no. 103.

Mulder V.L., Plötze M., de Bruin S., Schaepman M.E., Mavris C., Kokaly R.F., Egli M. (2013) Quantifying

mineral abundances of complex mixtures by coupling spectral deconvolution of SWIR spectra (2.1–2.4 μm) and regression tree analysis, Geoderma, Volumes 207–208, Pages 279-290.

Pompilio L., M. Sgavetti, and G. Pedrazzi (2007), Visible and near-infrared reflectance spectroscopy of pyroxene-bearing rocks: New constraints for understanding planetary surface compositions, J. Geophys. Res., 112, E01004, doi:10.1029/2006JE002737

Sack, R. O. & Ghiorso, M. S. 1994. Thermodynamics of multicomponent pyroxenes: II. Phase relations in the quadrilateral. Contributions to Mineralogy and Petrology 116, 287–300.

Schade Ulrich and Richard Wasch (1999) Near-infrared reflectance spectra from bulk samples of the two Martian meteorites Zagami and Nakhla, Meteoritics & Planetary Science 34, 417-424.

Shearer, C., Burger, P., Papike, J., McCubbin, F. & Bell, A. (2015) Crystal chemistry of merrillite from Martian meteorites: mineralogical recorders of magmatic processes and planetary differentiation, Meteoritics & Planetary Science 50, 649–673.

Spry A. (2013) Metamorphic Textures, reprint, revised, Elsevier, 358 pages.

Stöffler D., Ostertag R, Jammes C., Pfannschmidt G., Sen Gupta P.R., Simons M., Papike J.J., Beauchamp R.M. (1986) Shock metamorphism and petrography of the Shergotty achondrite. Geochimica et Cosmochimica Acta, 50, pp. 889-903

Treiman A. H., Gleason J. D., and Bogard D. D., (2000). The SNC meteorites are from Mars. Planetary and Space Science, 48, 1213-1230.

Taylor L. A., Nazarov M. A., Shearer C. K., Mcsween, H. Y. Jr., Cahill J., Neal C. R., Ivanova M. A., Barsukova L. D., Lentz R. C., Clayton R. N. and Mayeda T. K.(2002) Martian meteorite Dhofar 019: A new shergottite, Meteoritics & Planetary Science 37, 1107–1128.

Vago J.L., Westall F., Coates A.J., *et al*. Habitability on Early Mars and the Search for Biosignatures with the ExoMars Rover. Astrobiology. 17 (6-7):471-510. doi:10.1089/ast.2016.1533,2017.

Vaughan D.J. and Craig J.R., (1978), Mineral Chemistry of Metal Sulfides, Cambridge U. Press.

Yamaguchi, A., and Sekine T., (2000) Monomineralic mobilization of plagioclase by shock: An experimental study. Earth and Planetary Science Letters, 175, 289–296.

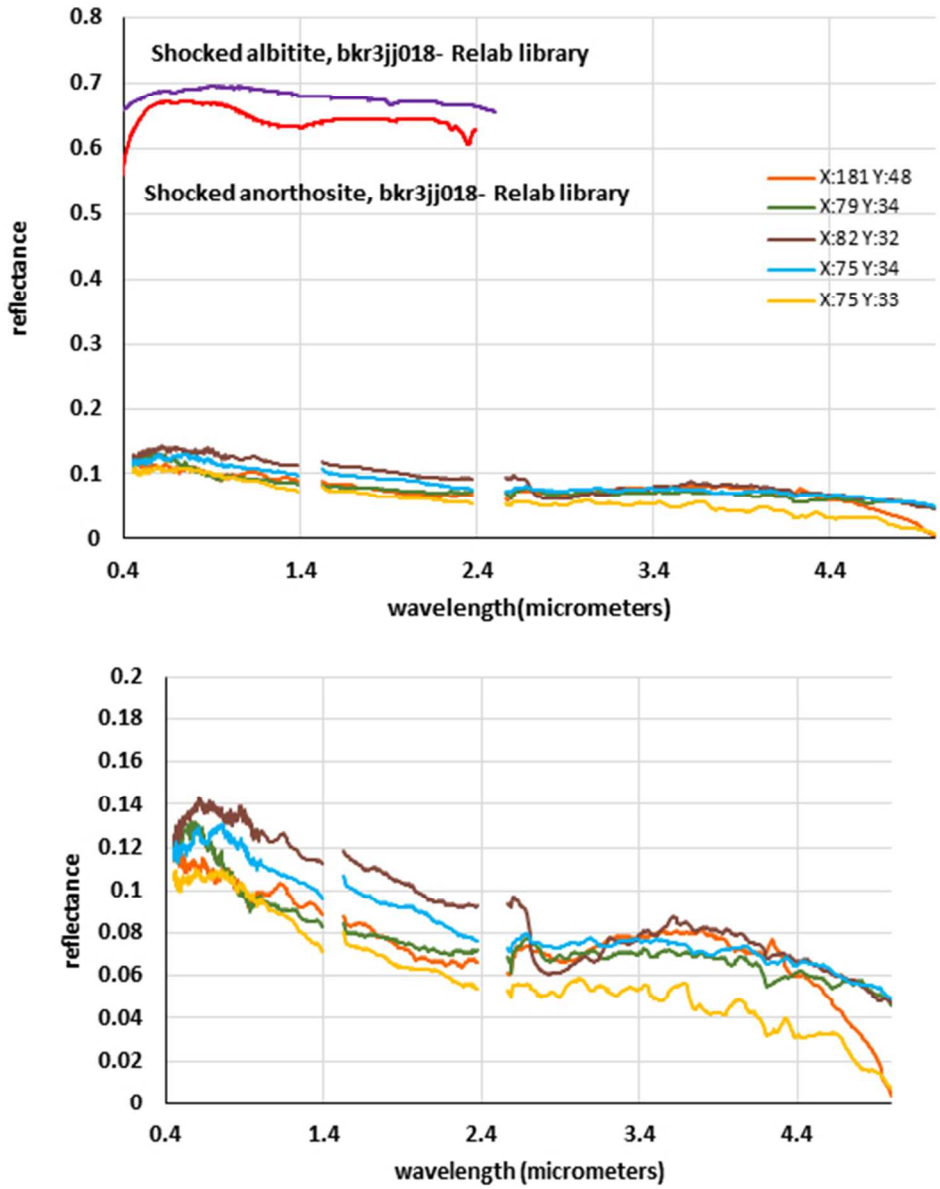

Fig.6. a) SPIM spectra of maskelynite grains in NWA8657 and comparison with shocked albitite and shocked anorthosite (Johnson and Horz, (2003. X and Y are the coordinates corresponding to the different pixels. Data around 1.5 and 2.5μm were removed because of instrumental artifacts; b) Zoom of the maskelynite spectra in Fig.6a

148x180mm (96 x 96 DPI)

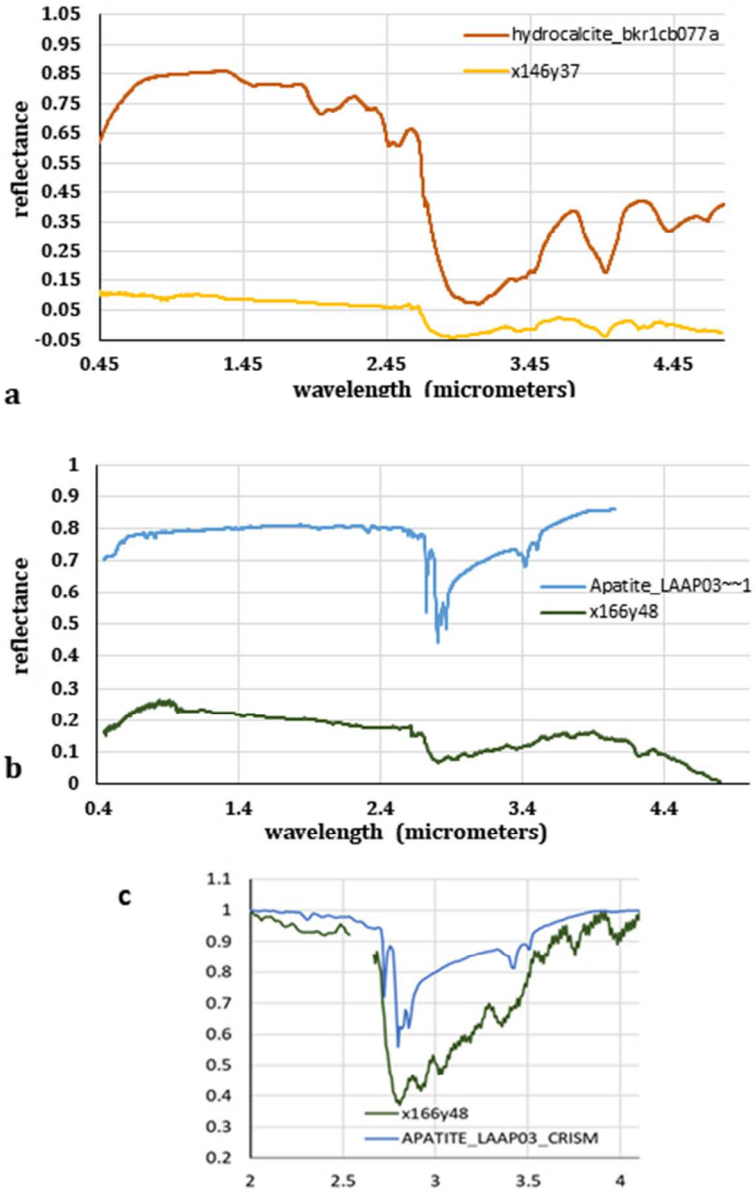

Fig.8a-b-c. a) Spectra of hydrated carbonates (146, 37) and hydrocalcite from Relab library. b) Spectra of phosphate phase (166,48) and apatite from CRISM library. X and Y are the coordinates corresponding to the different pixels. Data around 1.5 and 2.5μm were removed because of instrumental artifacts. c)Zoom of the continuum removed spectra in fig.8b in the range between 2 and 4.1μm

131x190mm (96 x 96 DPI)